Numerical Simulations of Blast Loads and Structural Deformation from Near-Field Explosions in Air

Björn Zakrisson, Bengt Wikman, Hans-Åke Häggblad

Accepted Manuscript

Title: Numerical Simulations of Blast Loads and Structural Deformation from Near-Field Explosions in Air

Authors: Björn Zakrisson, Bengt Wikman, Hans-Åke Häggblad

PII: S0734-743X(11)00020-0

DOI: 10.1016/j.ijimpeng.2011.02.005

Reference: IE 1978

To appear in: *International Journal of Impact Engineering*

Received Date: 28 May 2010

Revised Date: 17 December 2010

Accepted Date: 14 February 2011

Please cite this article as: Zakrisson B, Wikman B, Häggblad Hans-Åke. Numerical Simulations of Blast Loads and Structural Deformation from Near-Field Explosions in Air, International Journal of Impact Engineering (2011), doi: 10.1016/j.ijimpeng.2011.02.005

Title:
Numerical Simulations of Blast Loads and Structural Deformation from Near-Field Explosions in Air

Björn Zakrisson[a,b]
Bengt Wikman[a]
Hans-Åke Häggblad[b]

[a] BAE Systems Hägglunds AB, SE-891 82 Örnsköldsvik, Sweden
bjorn.zakrisson@baesystems.se
bengt.wikman@baesystems.se

[b] Luleå University of Technology, Solid mechanics, SE-971 87 Luleå, Sweden
Hans-Ake.Haggblad@ltu.se

Corresponding author:
Björn Zakrisson
BAE Systems Hägglunds AB, SE-891 82 Örnsköldsvik, Sweden,
bjorn.zakrisson@baesystems.se
Phone: +46 660 80824
Fax: +46 660 77453

Abstract

Numerical simulations of air blast loading in the near-field acting on deformable steel plates have been performed and compared to experiments. Two types of air blast setups have been used, cylindrical explosive placed either in free air or in a steel pot. A numerical finite element convergence study of the discretisation sensitivity for the gas dynamics has been performed, with use of mapping results from 2D to 3D in an Eulerian reference frame. The result from the convergence study served as a foundation for development of the simulation models. Considering both air blast setups, the numerical results under predicted the measured plate deformations with 9.4-11.1 %. Regarding the impulse transfer, the corresponding under prediction was only 1.0-1.6 %. An influence of the friction can be shown, both in experiments and the simulations, although other uncertainties are involved as well. A simplified blast model based on empirical blast loading data representing spherical and hemispherical explosive shapes has been tested as an alternative to the Eulerian model. The result for the simplified blast model deviates largely compared to the experiments and the Eulerian model. The CPU time for the simplified blast model is however considerably shorter, and may still be useful in time consuming concept studies.
All together, reasonable numerical results using reasonable model sizes can be achieved from near-field explosions in air.

Keywords:
Near-field, Blast load, Numerical simulation, High explosive, Convergence study

1. Introduction

It is in the near-field region a military vehicle is subjected to blast loading from of a buried land mine. Live land mine tests of military vehicles often follows the NATO standard [1], where the land mine may either be buried in sand or placed in a steel pot. Gel'fand et al. [2] stated that if the characteristic dimension of the charge is taken to be r_0, the extent of the near-

field region R_n is in the range $0 < R_n < 20r_0$. For a spherical charge of 0.75 kg and density 1500 kg/m^3 with radius r_0, the near-field region extends to about 1 meter from the explosive centre. In the near-field, the detonation products expand rapidly, reaching very high pressures and temperatures. This makes it usually difficult to measure for example pressure history in this region. However, it has for example been done by Esparza [3]. Much work regarding blast load characteristics is based on TNT data. Kingery and Bulmash [4] presented a collection of TNT data for spherical and hemispherical explosive shapes placed in air or on ground, covering a wide range of charge sizes and stand-off distances. Conwep is an implementation of the empirical blast models presented by Kingery and Bulmash, which is also implemented in the commercial hydrocode LS-DYNA based on work done by Rahnders-Pehrson and Bannister [5,6]. This makes it possible to simulate blast loads acting on structures representing spherical and hemispherical explosive shapes of TNT with reasonable computational effort. The Conwep loading model has for instance been used by Neuberger et al. [7], with satisfactory results regarding maximum plate deformations. However, the geometry of the explosive is of importance. Wenzel and Esparza [8] shows that a cylindrical Comp B explosive with diameter to thickness ratio of 3.25 can result in normally reflected specific impulses of up to 5 times that of a corresponding spherical shaped explosive with the same mass. Limited data is available to create empirical load functions with explosive shapes deviating from spherical. Further, if the explosive is confined in any way the determination of the load acting on a structure would be even more difficult and less generalized.

Nurick et al. [9,10] used an approach where the transferred impulse was directly measured in the experiments. From the impulse, the pressure could be calculated knowing the affected area and assuming the time duration of the pressure wave. The impulse load could thus be applied directly on the affected area of the structure in the calculations.

When the setup of the problem makes it unsuitable to use empirical load functions, an appealing approach may be to use a numerical hydrocode to calculate the build-up of the blast load. Air and the detonation products may be described with continuum mechanics in a gaseous domain, while the structure response is treated in a structural domain. An algorithm for the fluid-structure interaction is then used to connect the two domains. This has been done for example by Chafi et al. and Neuberger et al. [11,12]. Karagiazova et al. [13] made use of a combination between simulating the blast load and using an empirical load curve. In an initial 2D analysis, the blast load from a cylindrical charge was calculated in a gaseous domain storing the pressure history in space and time. The numerical result was then used to create an empirical relation of the pressure profile to be used onto the structure.

High demands rely on the user to validate the methods and parameters used to simulate the blast load and the structural response. Zukas and Scheffler [14] presented an example of an air blast loading problem performed independently by four different users using the same code, where each user's result deviated considerably from each other. Therefore, it is of essence that a model describing a dynamic event such as mine blast is controlled against numerical convergence, in order to get an estimate of the numerical errors. Also, methods should if possible be validated against confident test results.

Experiments and preliminary simulations regarding a detonating explosive in cylindrical shape acting on a deformable steel structure were carried out in half length scale in Zakrisson et al. [15], while additional experimental data is presented here. Explosive placement in both free air and in a steel pot is considered. When mine blast tests of military vehicles is performed according to the NATO standard [1], explosive placement in a steel pot is suggested as an alternative instead of explosive placement in the ground. This work will focus on the numerical calculations describing these blast events, which includes a convergence study of the gaseous blast load calculations along with comparison to experimental data. As

an alternative to the more advanced gaseous blast load description, the simpler empirical blast load description Conwep is tested and compared, both against results and CPU time.

2. Experiments

Blast experiments in air have been performed in order to collect data for numerical validation. In one experimental setup the explosive was placed in free air (air blast), while another experiment regarded explosive placed in a steel pot located on the ground (ground blast). Common for both experiments is that a blast load acted on a deformable steel target plate with thickness 8 mm and dimensions 600x600 mm. Weldox 700E was chosen as target plate, mainly due to available material characterisation from the literature to be used in the numerical simulations [16]. The explosive type was plastic explosive m/46 (commercially known as NSP 71), consisting of 86% PETN and 14% fuel oil, with a density of 1500 kg/m^3. The charge shape was cylindrical with diameter to thickness ratio of 3 and total weight 0.75 kg, with initiation in the centre.

2.1 Air blast

In order to study the response of square plates against an explosive located in air, a stiff test rig in steel was developed, described in detail with dimensions in Zakrisson et al. [15]. This air blast rig was used to perform tests on deformable target plates. The experimental setup is shown in Figure 1, where the target plate is simply supported on top of the rig and allowed to deform into the centre. The inner radius of the air blast rig is 250 mm, where the edge is smoothed with a 15 mm radius. The explosive charge was distanced with 250 mm stand-off from the target plate with a tripod of wood, see Figure 1a. A nonel fuse with a blasting cap was used to initiate the explosive at the centre. In Figure 1b, a crushable test gauge consisting of an aluminum honeycomb block is shown inside the air blast rig. The crush gauge was vertically mounted at the centre, distanced from the bottom surface of the target plate. The crush gauge deforms when the deforming plate comes in contact, allowing the maximum dynamic displacement of the target plate, δ_{max}, to be determined after the test. The inner edge of the air blast rig leaves a circular mark on the plate after the deformation, see Figure 2, which was used as reference to determine the vertical residual deformation. Since a square plate deforms into a circular hole, different bending modes arise perpendicular to the sides and along the diagonals of the plate. The residual deformation was measured vertically from the circular edge mark to the plate centre at the marker points shown in Figure 2, both to the sides, δ_{rs}, and along the diagonals, δ_{rd}. The average value of all measured δ_{rs} and δ_{rd} then represent the final residual deformation at the centre, δ_{res}.

Figure 1. Experimental setup for the air blast. In a), the target plate is simply supported on top of the air blast rig with the distanced cylindrical explosive. In b), the crush gauge is mounted inside the centre of the rig.

Figure 2. Deformed target plate viewed from below, showing the points for determining the residual deformation.

All together, 10 tests were performed; 5 tests with dry surface contact conditions between plate and rig, 5 tests with lubricated surfaces. The tests with lubricated surfaces were performed in order to get an estimate of the influence of friction, where the lubrication consisted of an S 75W-90 transmission oil with extreme pressure (EP) additive certified for

API GL-5. The experimental results are shown in Table 1, together with corresponding average values with extended subscript *ave*.

Table 1. Experimental results for the air blast experiments.

Surface	Test#	δ_{max} (mm)	$\delta_{max,ave}$ (mm)	δ_{res} (mm)	$\delta_{res,ave}$ (mm)
	1	63.9		56.2	
	2	66.9		58.3	
	3	66.3		58.5	
	4	66.8		59.0	
Dry	5	65.6	65.9	57.7	57.9
	6	66.4		59.0	
	7	67.9		60.3	
	8	67.1		60.5	
	9	66.4		59.8	
Lubricated	10	65.9	66.7	58.2	59.6

2.2 Ground blast

In an earlier work, a test rig to allow explosive positioning in sand or a steel pot was developed to include measurement of momentum transfer in addition to structural deformation [15]. One aim of the experiments was to replicate conditions of the NATO standard [1], where an explosive located in a steel pot is suggested as an alternative test method instead of positioning in sand. The experiments were performed in half length scale compared to the standard. The experimental setup is shown in Figure 3 and is explained in more detail in Zakrisson et al. [15], together with results from a total of 10 tests with sand and 2 tests with steel pot. However, the only setup considered in the present study is the steel pot. A test module is hanging in chains, free to move upwards from the blast. The test module consists of ballast weights, the air blast rig described in section 2.1 mounted upside down, a target plate and a plate holder. The total weight of the test module is 2120 kg.

Figure 3. The ground blast rig to the right, with test module hanging in chains and steel pot placed underneath. To the left, the test module is viewed from underneath, where the target plate is held in place with a plate holder.

The target plate was held against the test module during the blast by a plate holder in steel, with the essential dimension shown to the left in Figure 3. Only dry contact surfaces were used in the experiments. The cylindrical steel pot was made with an outer diameter of 350 mm and height 150 mm, with a countersunk hole with radius 87 mm and depth 66 mm with the bottom edge smoothed with a 25 mm radius. The cylindrical explosive was distanced 25 mm from the bottom of the steel pot with extruded polystyrene foam, which was considered to have negligible influence on the test. The stand-off distance from the top surface of the charge to the surface of the target plate was 255 mm. The maximum dynamic- and residual plate deformation, δ_{max} and δ_{res}, were determined in the same way as described in section 2.1. Further, the maximum vertical displacement of the test module, Z_{tm}, was determined both using a crush gauge and a linear position sensor, shown on top of the test module to the right in Figure 3. The crush gauge only gives the maximum position of the test module translation. The position sensor however, registers the vertical movement of the test module in time. The two methods in determining Z_{tm} result in a deviation of the transferred impulse of 0.6% and 2.8% for the two tests using the steel pot. However, the overall experience considering all 12

tests (both sand and steel pot) was that the two measurement methods were working equally well [15]. Thus, the results of the test module jump for both methods is given in Zakrisson et al. [15], while here only an average value is presented. By assuming vertical translation only and that the initial velocity equals the maximum velocity, the total impulse transferred to the test module may be estimated from the maximum vertical movement as

$$I_{tm} = m\sqrt{2gZ_{tm}}\,, \tag{1}$$

where m is the total mass of the test module and g is the gravity constant.
Two tests using steel pot were performed, where the experimental results from Zakrisson et al. [15] along with the calculated impulse using Eq. (1) are given in Table 2.

Table 2. Results for ground blast experiments with explosive placed in steel pot.

	Target plate		Test module	
Test	δ_{max} (mm)	δ_{res} (mm)	Z_{tm} (mm)	I_{tm} (Ns)
11	124.5	108.6	60.0	2300
12	123.4	110.7	59.2	2285

3. Numerical methods

The general numerical methods used in this work to describe the blast loading and structural deformation are described in this section. The explicit finite element (FE) hydrocode LS-DYNA V971 R4.2.1 [6] was used for the calculations. All numerical simulations in this work were performed on a Linux SMP cluster with 8 Gb of available memory. Only one core was used on a 2.8 GHz dual core AMD Opteron 2220 processor, with double precision.

3.1 Reference frame

A structure is generally easiest defined in a Lagrangian reference frame where the mesh follows the material movement. The drawback is when the element gets too distorted due to large deformations. This could result in reduced accuracy, smaller time steps and possible solution failure. An alternative is the Arbitrary Lagrangian-Eulerian (ALE) method, where the boundary of the part still remains the Lagrangian reference. Within the part the mesh is controlled against distortion and does not necessarily follow the material movement. The element nodes are moved in order to remain accuracy and stable solutions, and the material state variables are thus advected to the new, smoother mesh. Different advection methods for the material transport may be used. Generally when advection is used, both momentum and kinetic energy is not conserved at the same time. Commonly, momentum and internal energy is conserved but not kinetic energy. The consequence is usually that the kinetic energy decreases in time, hence also the total energy [6,17]. Another drawback with the ALE method may be increased computational time due to the advection. Depending on the problem however, advection when using ALE may not be needed every time step which reduces the computational effort. Another approach is the Eulerian reference, where the nodes are completely moved back to the original position after the material advection. An extension of the Eulerian approach is the Multi-Material ALE (MMALE), where one single element may contain several different materials, with tracked material interfaces. This is an appealing method for describing the gas flow from detonating explosives, where the gradients are large. However, much of the computational cost in a hydrocode is associated with the treatment of elements containing more than one material [17]. Also, many small elements must be used to achieve sufficient accuracy in order to minimise the advection error, on the expense of computation time [18]. In the main part of this work, both a Lagrangian and an Eulerian domain are used, together with a coupling algorithm to connect the two domains. The

Lagrangian domain consists of the structural materials while the Eulerian domain is modelled with MMALE elements and mainly used for gaseous materials such as air and explosive.

3.2 Shock

A shock front is extremely thin, and therefore often approximated as a discontinuous change in flow properties. The shock front thickness is normally much thinner than a typical finite element length used in a problem of practical use. Special treatment is used in numerical codes in order to solve the discontinuity and still keep conservation of mass, momentum and energy across the shock front, i.e. the Rankine-Hugoniot conservation relations for shock waves. In order to treat the shock numerically, artificial viscosity is used [19]. A viscous term is added to the pressure in both the energy and momentum equations to smear out the shock front over several elements. The artificial viscosity is only active at the shock front, and transforms the actual discontinuity to a steep gradient, spread over a couple of elements [20].

3.3 Contact

The contact definition between two Lagrangian parts used in this work is based on a penalty method, independent of the normal direction of the shell elements. A friction model based on the Coulomb formulation is included in the contact algorithm [20].
The contact coupling between the gaseous materials in the Eulerian domain to the structures in the Lagrangian domain is defined with a fluid-structure interaction (FSI) algorithm. In this work, a penalty based method is used. The method conserves energy and applies nodal forces explicitly by tracking the relative motion of a given point [11]. When a fluid particle penetrates a Lagrangian element, a penalty force is applied to both the fluid particle and the Lagrange node to prevent penetration. The penalty factor may be defined as a user defined curve representing penalty pressure against penetrated distance [6].

3.4 Mapping from 2D to 3D

The technique of mapping results from 2D to 3D in an Eulerian domain has been available in the hydrocode Autodyn for several years [21,22], and recently implemented in LS-DYNA (V971 R4) [6,23]. The purpose of using mapping is to save computational time and increase the accuracy since the resolution in 2D may be much higher than a corresponding 3D model due to computational limitations. The work flow when using mapping is to perform an axi-symmetric simulation in 2D until the velocity field is close to the boundary, where the symmetry condition would be violated. At the last cycle, a binary map file is written, containing the state variables of the 2D Eulerian domain. The map file is then used to fill the 3D Eulerian domain as initial condition, where the calculation continues. Mapping may also be used from 2D to 2D. Aquelet and Souli illustrates the mapping technique of LS-DYNA in [23], with identical element size in 2D and 3D. The benefit is then to save computational time by reusing the map file if identical initial calculations are to be used in several simulation cases. The sensitivity of using mapping with LS-DYNA from an initial 2D model with fine element resolution to a subsequent 2D model with coarser element resolution was investigated by Lapoujade et al. in [24]. It was concluded that compared to the initial model the peak pressure becomes smeared out and drops about 10% with element size ratio of 10 between the subsequent and initial element size, respectively. The specific impulse however remains relatively constant until element size ratio of 20.
However, a fine mesh for the initial 2D simulation and a coarser mesh for the subsequent 3D simulation will still result in increased accuracy compared to a corresponding single 3D solution with coarse mesh.

3.5 Empirical blast load function

The empirical blast loading function CONWEP, based on TNT data from Kingery and Bulmash [4], was implemented in LS-DYNA based on work by Randers-Pehrson and Bannister [5,6]. This enables an opportunity to simulate blast loading on a Lagrangian structure without having to simulate the blast load in an Eulerian domain. The blast load corresponds to either free air detonation of a spherical charge or surface detonation of a hemispherical charge of TNT. The load acts on a set of predefined segments, i.e. a surface of solid elements or shell elements. The pressure p that acts on a segment account for angle of incidence of the pressure wave, θ, is determined according to

$$p = p_i \cdot \left(1 + \cos\theta - 2\cos^2\theta\right) + p_r \cdot \cos^2\theta, \tag{2}$$

where p_i is the incident pressure and p_r the reflected pressure [5]. However, no shadowing, confinement or tunnel effects are included in the blast loading model.

4 Material models

The models and parameters used to describe the structural and gaseous materials are presented in this section. The units used in the simulations are for the length, time and pressure given in *cm*, μs and *Mbar*. However, the material parameters are here given in more convenient units in the tables.

4.1 Gaseous materials

The explosive is modelled as a high explosive material with a Jones-Wilkins-Lee (JWL) form of equation of state. A combined programmed burn and beta burn model determines when an explosive element is detonated based on the initial density ρ_0, detonation pressure P_{CJ} and detonation velocity D [6]. The programmed burn model defines at what time an explosive element is detonated based on a given detonation point and the detonation velocity. The beta burn model allows an explosive element to be detonated due to compression, i.e. when the pressure in an explosive element reaches P_{CJ}. When the criteria for detonation of an explosive element is achieved based on either the programmed- or beta burn model, the energy is then released with the pressure defined according to the three term JWL equation of state as

$$p = A \cdot \left(1 - \frac{\omega}{R_1 \cdot v}\right) e^{(-R_1 \cdot v)} + B \cdot \left(1 - \frac{\omega}{R_2 \cdot v}\right) e^{(-R_2 \cdot v)} + \frac{\omega \cdot E}{v}, \tag{3}$$

where A, B, R_1, R_2 and ω are material constants, $v = \rho_0/\rho$ is the relative volume and E is the internal energy per unit reference volume. The constants are usually empirically determined with cylinder tests or in combination with thermo chemical simulations of the reaction products. The JWL equation of state for the plastic explosive m/46 used in the experiments in section 2 have been calibrated and validated using cylinder tests presented in a report by Helte et al. [25]. The material- and JWL parameters for m/46 are given in Table 3.

Table 3. Material- and JWL-parameters for the plastic explosive m/46 [25].

ρ	D	P_{CJ}	A	B	R_1	R_2	ω	E_0
kg/m^3	m/s	GPa	GPa	GPa	-	-	-	kJ/cm^3
1500	7680	21.15	759.9	12.56	5.1	1.5	0.29	7.05

The air is modelled with an ideal gas form of equation of state, defined as

$$p = (\gamma - 1)\frac{\rho}{\rho_0} E, \tag{4}$$

where ρ is the current density and ρ_0 the initial density while E is the internal energy per unit reference volume. Also, γ is defined as the ratio between the specific heat at constant pressure and volume, respectively, where γ=1.4 at small overpressures. At larger pressures and higher temperatures, the air starts to ionize and dissociate, and the property of the gas changes so the ratio of specific heats is no longer constant [26]. Albeit high overpressures will be reached in the near-field, it is here assumed that γ=1.4 is sufficiently accurate. With initial density 1.169 kg/m^3, the initial pressure is 1 bar which results in an initial internal energy E_0 of 250 kJ/m^3 [27].

4.2 Structural materials

A common model used to describe materials subjected to large deformation, high strain rate and adiabatic temperature softening is the Johnson and Cook (JC) model. The model is based on von Mises plasticity, where the yield stress is scaled depending on the state of equivalent plastic strain, strain rate and temperature. A modified JC model is described by Børvik et al. in [28], where the equivalent yield stress is defined as

$$\sigma_{eq} = \left(A + B\varepsilon_{eq}^{n}\right)\left(1 + \left[\dot{\varepsilon}_{eq} \Big/ \dot{\varepsilon}_0\right]\right)^{C}\left(1 - T^{*m}\right), \tag{5}$$

where A, B, n, C and m are material constants, $\dot{\varepsilon}_{eq}$ and $\dot{\varepsilon}_0$ are the equivalent plastic- and reference strain rate, respectively. The homologous temperature, T^*, is defined as $T^*=(T-T_r)/(T_m-T_r)$, where T is the current temperature, T_r the room- or initial temperature and T_m the material melting temperature. The temperature increment due to adiabatic heating is a function of the equivalent plastic strain increment, equivalent stress, specific heat, density and the Taylor-Quinney coefficient which represents the proportion of plastic work converted into heat.

In this work, the modified JC model is used for the steel plate Weldox 700E, which undergoes large plastic deformation. The material parameters for Weldox 700E regarding the modified JC model is given by Børvik et al. in [16], shown in Table 4. The strain rate parameters $\dot{\varepsilon}_0$ and C has been adjusted to this work to better correlate the model response with the experimental strain rate experiments presented in [16]. The strain rate dependence for Weldox 700E was evaluated at 3% plastic strain, and is shown in Figure 4 together with the Johnson-Cook model response with the modified material parameters from Table 4. The reference strain rate $\dot{\varepsilon}_0$ is set to 1 s^{-1}, while the material constant C is determined by letting the model response pass through the last experimental value. The temperature dependence was not tested experimentally but estimated by letting material constant m be equal to 1, which appears to be a reasonable assumption for steels [16].

Table 4. Weldox 700E material constants for the modified JC constitutive model [16].

Yield stress	Strain hardening		Strain rate		Temperature softening		
A (MPa)	B (MPa)	n (-)	$\dot{\varepsilon}_0$ (s^{-1})	C (-)	T_r (K)	T_m (K)	m (-)
819	308	0.64	1[a]	0.0221[a]	293	1800	1

Elastic constants		Density	Temperature related coefficients		
E (GPa)	ν (-)	ρ (kg/m^3)	C_p (J/kg-K)	χ (-)	α (K^{-1})
210	0.33	7850	452	0.9	1.2×10^{-5}

[a.] Modified values compared to reference.

Figure 4. Equivalent stress at different various strain rates, evaluated at 3 % plastic strain. Experimental values from reference [16] is shown together with the response of the modified JC model with adjusted strain rate parameters.

5 Convergence study

A numerical convergence study of the gas flow interacting with air and a rigid surface was performed in order to study effect of model discretization. The problem was isolated to only include the gas dynamics, by using successively smaller elements in the Eulerian domain. Initial 2D simulations were performed until the shock wave almost reached the boundary. The result was thereafter mapped to coarser 3D meshes, where the simulation continued.
For the material transport in the MMALE elements, the 2nd order accurate van Leer method is used [20]. Also, an area weighted residual is used for the axi-symmetric 2D elements.

5.1 Uniform element size

Figure 5. Schematic picture of the initial 2D model at time 0 to the left, subsequent 3D model after mapping from 2D at time 56 μs to the right. The explosive material expansion is shown in dark colour. Note that y-direction in 2D equals z-direction in 3D.

The domain size is chosen to represent the air blast experiment described in section 2.1, and shown in Figure 5 for both the 2D axi-symmetric and the 3D model, which is modelled in quarter symmetry. The explosive is m/46, represented by a total of 0.75 kg with a diameter to thickness ratio of 3 and material parameters according to Table 3. Only half of the explosive height is modelled, with use of symmetry. This gives a 250 mm stand-off distance between the top surface of the explosive and the upper boundary, identical to the air blast experiment. Prevented outflow is defined as $\partial u_i/\partial t = 0$, where $\partial u_i/\partial t$ is the velocity in the direction i normal to the boundary. As shown in Figure 5, prevented outflow apply at all boundaries in the 2D model as well as the three symmetry planes for the 3D model, along with the rigid top boundary. For the 3D model, the outer lateral boundaries have free outflow. At the rigid top boundary, sampling points for the pressure are placed radially from the vertical symmetry axis r_0=0 mm with 10 mm interval to r_{300}=300 mm along the xz symmetry plane, shown in Figure 5. The 2D calculation runs to the simulation end time $t_{end}^{2D} = 56$ μs, when a map file is written containing the field of the state variables representing the explosive and air. The 2D solution is then mapped into the 3D MMALE mesh as an initial condition. Since $t_{end}^{2D} = 56$ μs

for the initial 2D simulation, this becomes the start time in the 3D simulation. The 3D simulation end time is $t_{end}^{3D} = 600$ μs, in order to include the complete positive overpressure phase for all sampling points, i.e. until $p_r\left(t_{end}^{3D}\right) < p_0$, where p_r is the pressure at the radial sampling point r and p_0 is the initial air pressure. The pressure time histories are then integrated with respect to time to get the reflected specific impulse, i, in units (Pas). The maximum reflected specific impulse at each sampling point $r=r_0$ to r_{300} is then

$$i_r = \max\left(\int_{t_0}^{t_{end}^{3D}} p_r dt\right). \tag{6}$$

By integrating i_r over the radius and the radial area (i.e. around the revolving axis), a curve for the total accumulated impulse in units (Ns) on a circular surface is constructed according to

$$I_{tot} = 2\pi \cdot \int_{r_0}^{r_{300}} i_r \cdot r dr. \tag{7}$$

The total accumulated impulse, I_{tot}, over a rigid circular area at radius r_{300}=300 mm is thus the chosen quantity for the convergence evaluation.

The recommended procedure for estimation of the discretization error given by Celik et al. [29] is followed. This procedure is based on the Richardson extrapolation and determines the Grid Convergence Index (GCI). First, a representative mesh size h is defined. In this section, only uniform meshes are used, both in 2D and 3D. The element side length is the chosen h_n, where n=1,2,3 and defined as $h_1<h_2<h_3$. The three subsequently coarsened sets of meshes are simulated, where a key solution f_n, in this case $I_{tot,n}$ from Eq. (7), is determined for each individual solution n. The grid refinement ratios are $r_{21}=h_2/h_1$ and $r_{32}=h_3/h_2$. Since $h_3=2h_2=4h_1$ in this study, the grid refinement ratio is constant, i.e. $r=2$. The order of convergence, p, with constant r is defined as

$$p = \frac{\left|\ln\left(\left|\frac{f_3 - f_2}{f_2 - f_1}\right|\right)\right|}{\ln(r)}. \tag{8}$$

The extrapolated asymptotically exact solution according to Richardson extrapolation may then be written as

$$f_{ext} = f_1 + \frac{(f_1 - f_2)}{(r^p - 1)}. \tag{9}$$

The approximate relative error ε_a for the two finest grid solutions is defined as

$$\varepsilon_a = \left|\frac{f_1 - f_2}{f_1}\right| \tag{10}$$

and the extrapolated relative error ε_{ext} is defined as

$$\varepsilon_{ext} = \left|\frac{f_{ext} - f_1}{f_{ext}}\right|. \tag{11}$$

The fine grid GCI is defined as

$$GCI = \frac{F_s \cdot \varepsilon_a}{(r^p - 1)}, \tag{12}$$

where F_s is a safety factor multiplying the approximate relative error term ε_a. When three or more grids are used in the determination of the GCI, then F_s = 1.25. The safety factor is used to get a conservative estimate of the GCI, and should be thought of as representing a 95% confidence bound on the approximate relative error [30]. The GCI then provides an estimate of the amount of discretization error in the finest grid solution relative to the converged numerical solution.

Three 2D meshes with element lengths 0.25 mm, 0.5 mm and 1.0 mm are termed Case 1, 2 and 3. The results for each 2D solution is mapped to three 3D meshes with h_1=4 mm, h_2=8 mm and h_3=16 mm, where I_{tot} for each solution is determined. The results along with the corresponding GCI is calculated and reported in Table 5, where the relative terms have been converted to percent. Case 2, with a 2D mesh of 0.5 mm show the lowest GCI of ±2.13 %.

Table 5. GCI with total accumulated impulse over a cylindrical surface.

Case	Mesh size (mm) 2D	3D			Solutions (Ns)				(-)	(%)	(%)	(%)
		h_1	h_2	h_3	$I_{tot,1}$	$I_{tot,2}$	$I_{tot,3}$	$I_{tot,ext}$	p	ε_a	ε_{ext}	GCI
1	0.25	4	8	16	659	618	527	694	1.14	6.27	4.97	6.54
2	0.5	4	8	16	653	628	547	664	1.69	3.82	1.68	2.13
3	1.0	4	8	16	646	599	525	726	0.67	7.25	11.00	15.45

The total impulse for Case 2 is shown in Figure 6a, plotted at each mesh size in terms of the 3D fine grid size h_1=4 mm. Also, the GCI error bar for the fine grid is shown along with the extrapolated exact solution $I_{tot,ext}$ at infinitesimal element length. The graph illustrates the impulse convergence with smaller mesh size in the 3D domain. In Figure 6b, the reflected specific impulse *i* for Case 2 is plotted against the radius *r*, where a localisation effect with higher specific impulse is shown closer to the symmetry axis. Also, a single 3D solution with mesh size h_1=4 mm without initial mapping from 2D is shown. This result indicates that the 3D solution is approximately equal to Case 2 with 8 mm mesh size in the 3D model, and illustrates the strength of mapping from a 2D model with higher resolution.

Figure 6. Convergence results for Case 2, with 0.5 mm 2D mesh. In (a), the accumulated impulse, I_{tot}, is shown for each mesh size in terms of the fine grid size, together with the GCI error bound for the fine grid solution and the extrapolated exact solution, h_{ext}. In (b), the reflected specific impulse, *i*, is plotted against the radial distance from the symmetry axis, together with a single 3D solution for h_1=4 mm without mapping from 2D.

5.2 Non-Uniform element size

Figure 7. The reflected specific impulse, *i*, is plotted against the radial distance from the symmetry axis. Initial 2D simulation with 0.5mm uniform element size is mapped to 3D models with uniform element size 4 mm and element bias distribution of 3, respectively.

In an attempt to reduce the number of elements needed in the model, without reducing the accuracy of the solution, a simulation with non-uniform element size is performed. The initial 2D mesh had a uniform element side length 0.5 mm, i.e. identical with Case 2 used in section 5.1. The 3D domain size was identical as shown in Figure 5. However, the element

distribution in the 3D model varied. In total, 40 hexagonal elements were used in all three directions, resulting in 64000 elements. With Figure 5 in mind, the element side length was biased with 3, with smaller element lengths vertically towards the rigid top surface and laterally towards the symmetry axis. The reflected specific impulse distribution against the radial direction is shown in Figure 7, both for the 4 mm uniform 3D mesh together with the biased mesh. The specific impulse distribution is close to identical between the two models, but the total number of elements is about 10 times less for the non-uniform model compared to the uniform model. Hence, the CPU time and the memory allocation to solve the problem may in this way be significantly reduced without reducing accuracy.

6 Finite Element Models of Experimental Tests

The FE models describing the air- and ground blast experiments are presented in this section. Two variants of describing the blast load are used. The blast load is either simulated in an Eulerian gas domain with fluid structure interaction to the Lagrangian structure, or an empirical blast load function is used and applied on the affected Lagrangian surfaces. This section describes the Eulerian blast load model in detail, while the empirical blast load function (Conwep) is described in section 3.5. The model of the structural Lagrangian parts is identical irrespective of the blast load used. For all numerical simulations, the target plate Weldox 700E is modelled with the modified JC model with parameters given in Table 4. Only fully integrated shell elements with 5 through thickness integration points have been used for structural calculations in 3D, where also thickness change due to membrane stretching is accounted for. Regarding the blast load calculations using an Eulerian domain, the explosive consists of the plastic explosive m/46, described with the JWL equation of state with parameters given in Table 3. The total weight of the explosive is 0.75 kg, cylindrical in shape with diameter to thickness ratio of 3. When the Conwep blast load function is used, either spherical air burst or hemispherical surface burst of TNT may be used. In this work, the air burst is used for the air blast simulations, while the hemispherical surface burst is used for the ground blast simulations. The TNT equivalence for m/46 regarding the specific impulse was determined to 1.16 by Elfving in [31], which gives that 0.75 kg of m/46 is represented by 0.87 kg TNT when Conwep is used. No direct conversion factor between the difference in explosive shape, i.e. spherical compared to cylindrical, have been found in the literature, hence this effect is not accounted for. The point of detonation for the Conwep simulations is chosen so the stand-off measured from the surface of the explosive to the target plate is identical compared to the Eulerian blast load calculations using a cylindrical charge of m/46.

6.1 Air blast

The FE model discretization of the gas domain is based on the methodology used in the convergence study, with mapping of results from 2D to 3D. The model from section 5.1 replicated the setup for the air and explosive along with the stand-off distance used in the air blast experiment. The map file can therefore be reused from the initial 2D gas dynamic simulation with 0.5 mm element side length, with a total of 432259 elements. The initial 2D result is then mapped into a 3D gas domain shown in Figure 8, with dimensions given in Table 6. Note that when the Conwep blast load is used, the Eulerian domain in Table 6 is omitted.

Figure 8. The numerical Air blast model in quarter symmetry viewed from above, looking into the three symmetry planes of the Eulerian domain.

Table 6. Model details for the air blast.

Part	Material	Element type	Element side length (mm)	Number of elements	Model size		
					X-dir (mm)	Y-dir (mm)	Z-dir (mm)
Target plate	Weldox 700E	Shell	5	3600	300	300	-
Air blast rig	Rigid	Shell	2[a]	5684	300	300	-
Euler domain[b]	Air, m/46	MMALE	3.7[c]	96000	400	400	370

[a]Element size at the radius.
[b]Omitted for Conwep blast load.
[c]Minimum element size.

Figure 9. The XZ-view of the mesh distribution in the Eulerian domain is shown. Denser element distribution is located laterally towards the symmetry axis as well as vertically towards the position of the target plate. Bias B indicates the ratio of the largest/smallest element length across a distance.

The plate, rig and air are modelled in quarter symmetry, while the explosive is represented in 1/8 symmetry. As shown in Figure 8, similar symmetry conditions for the 3D gas domain as used in the convergence study are used, where three symmetry planes has prevented outflow; at the top of the model and the two planes along the centre axis of the explosive. Outflow is allowed on the outer lateral and bottom boundaries. In Table 6, the used material, element type and side length along with total number of elements are given, together with the model size for the target plate, air blast rig and the gas domain, respectively. The Eulerian domain size and the mesh distribution in the XZ-view is given in Figure 9. The element length bias ratio across a distance is defined as $B=L_{e,max}/L_{e,min}$, where $L_{e,max}$ and $L_{e,min}$ is the largest and smallest element side length respectively. The target steel plate consisted of shell elements with 8 mm thickness and located below the top boundary, at an initial 250 mm stand-off measured from the bottom of the explosive to the top of the plate. The plate is simply supported on a rigid surface, representing the air blast rig, with contact definition between the two surfaces. All nodes were fully constrained for the rig. An FSI-algorithm couples the blast load to the target plate. The 3D simulation is stopped after 1000 μs calculation time, when the FSI-force approximately reaches zero. To save CPU time, the MMALE elements are then deleted from the calculation, which continues to the final calculation time t_{end}=8000 μs, allowing the residual deformation of the plate to converge. In order to determine the maximum and residual deformation of the plate, the vertical displacement is stored for the plate middle node, $\delta_0(t)$. To determine the reference for the residual deformation, vertical displacements of the plate nodes at the position for the rig inner boundary (r=265 mm) is stored, both on the diagonal, $\delta_{rd}(t)$, and towards the side of the plate, $\delta_{rs}(t)$. Similar reference points were used to determine the residual deformation in the air blast experiment. The maximum dynamic deformation of the plate is determined as $\delta_{max}=\max(\delta_0(t))$, which occurs at time t_{max}. To determine the residual deformation, δ_{res}, a relative displacement for the nodes is determined by subtracting the average motion of the two nodes initially at the position of the rig inner boundary from the plate middle node motion, $\delta_{rel}(t)=\delta_0(t)-\delta_r(t)$, where $\delta_r(t)=\text{average}(\delta_{rd}(t),\delta_{rs}(t))$. This relative motion has to be determined since the plate bounces off the rig due to the elastic spring back. The residual deformation is then determined by averaging the displacement of the constructed relative displacement curve from the time of maximum deformation to the end time as $\delta_{res}=\text{average}(\delta_{rel})$ from t_{max} to t_{end}. This approach is illustrated in Figure 10.

Frictionless contact state is assumed. However, the influence of friction is tested with a constant friction coefficient of μ=0.1 and μ=0.2.

Figure 10. Method for determination of maximum and residual plate deformation.

6.2 Ground blast

The FE model discretization of the gas domain representing the ground blast experiment is based on the methodology with mapping presented in section 5. In contrast to the air blast experiment/simulation, where the explosive was placed in free air, the charge is here placed in a steel pot. The same stand-off distance as used in the experiment is used, i.e. 255 mm measured from the top surface of the explosive to the bottom surface of the plate. The use of the steel pot along with the fact that the structure for the ground blast is much larger than the air blast, lead to some differences in the modelling compared to the air blast.
The initial 2D model of the ground blast is shown in Figure 11, which consists of 2D axi-symmetric MMALE elements with air and explosive, with the boundary modelled to represent the steel pot. The rectangular model size above the explosive surface is 400x250 mm, while the inner shape representing the steel pot is identical as described for the ground blast experiment in section 2.2. The side length of the quadrilateral elements is uniform with 0.5 mm except the area of the smoothed bottom edge representing the steel pot, which has slightly smaller element length. The model consists of 422292 elements in total. Outflow is prevented on all boundaries for the 2D model. The simulation end time is 56 μs, when a mapping file to be used to initialize the 3D domain is written.

Figure 11. The 2D model of the ground blast with explosive placed in steel pot.

The 3D model representing the ground blast experiment is shown in Figure 12, modelled in quarter symmetry. The Eulerian domain consists of the gaseous material such as air and explosive, but also the steel pot. The structural Lagrangian domain consists of the rigid ground blast rig, plate holder and the target plate. A summary of the specific details for each part is given in Table 7. Note that when the Conwep blast load is used, the Eulerian domain in Table 7 is omitted. In order to get a more accurate result for the impulse transfer, the deflection plates at the top of the test module was modelled, shown in two views with dimensions in Figure 13. For comparison to the experimental ground blast rig, see Figure 3.

Table 7. Details for the ground blast 3D Model.

Domain	Part	Material	Element type	Thickness (mm)	Number of elements
Lagrange	Target plate	Weldox 700E	Shell	8	3600
	Plate holder	Weldox 700E	Shell	15	152
	Ground blast rig	Rigid	Shell	0.1	8428
Euler[a]	Air	Air	MMALE	-	365904
	Explosive	m/46	MMALE	-	
	Steel pot	Elastic steel	MMALE	-	4150[b]

[a]Omitted for Conwep blast load.
[b]Shell elements representing the steel pot to initialize the MMALE elements.

Figure 12. The numerical model in quarter symmetry of the ground blast experiment in the 3D domain, viewed from underneath.

Figure 13. Dimensions in mm specific to the numerical model of the ground blast rig.

Regarding the 3D Eulerian mesh for the ground blast model, smaller element sizes were used closer to the symmetry axis and towards the target plate, with coarser elements to the boundaries. This methodology is supported by section 5.2, and is also used for the air blast model. The Eulerian domain size and the mesh distribution in the XZ-view is given in Figure 14. The element length bias ratio across a distance is defined as $B=L_{e,max}/L_{e,min}$, where $L_{e,max}$ and $L_{e,min}$ is the largest and smallest element side length respectively. For the 3D model, outflow is prevented on the two symmetry planes and at the bottom surface, but allowed on the top and outward lateral boundaries. The Eulerian domain consists mainly of air and explosive, where the inner volume of the shell elements representing the steel pot shown in Figure 12 is only used to initialize the MMALE elements with elastic steel material. The number of elements to describe the steel pot is given in Table 7. The field of the state variables representing the gas from the 2D simulation is mapped into the 3D MMALE mesh as an initial condition, where the 2D simulation end time 56 μs is the start time in the 3D simulation.

Figure 14. The XZ-view of the mesh distribution in the Eulerian domain is shown. Denser element distribution is located laterally towards the symmetry axis as well as vertically towards the position of the target plate. Bias B indicates the ratio of the largest/smallest element length across a distance.

In the Lagrangian domain, the surface of the ground blast rig in contact with the steel plate is modelled with equal accuracy as for the air blast model, while larger elements were used elsewhere; see Figure 12. The model for the target steel plate is identical with the one used in the air blast simulations. The outer edges of the plate holder are connected to the rig, so the corner of the target steel plate is clamped against the rig, shown in Figure 12. No other load than the external blast load is applied on the plate holder in order to press the plate against the rig. The plate has a contact definition against both the rig and the plate holder, and will slide in between the two surfaces. An FSI-algorithm couples the blast load to the ground blast rig and the target plate. The ground blast rig is constrained in all directions except in the z-direction. A mass is applied on the rigid ground blast rig so the total mass of the test module is 530 kg, i.e. one quarter of the total test module weight 2120 kg used in the test. With a global gravity of 9.81 m/s^2, the test module is then allowed to translate vertically from the blast load, and return down as effect of the gravity. The maximum vertical displacement of the test module, Z_{tm}, is recorded in order to calculate the impulse transfer I_{tm} according to Eq. (1). Also, the impulse transferred to the Lagrange structures via the FSI, I_{FSI}, is calculated by integration of the total vertical FSI force over time.
The 3D simulation is stopped after 1500 μs calculation time, which is when the FSI-force approximately reaches zero. The MMALE elements are then deleted from the calculation, which continues to the time 8000 μs, allowing the residual deformation of the plate to converge. To reduce computation time, the deformable steel plate is then switched to rigid,

whereas the calculation continues to the end time 0.25 s in order to capture the maximum jump of the test module, Z_{tm}.
Regarding the plate deformation, the maximum dynamic deformation of the middle node, δ_{max}, along with the residual deformation, δ_{res}, is determined in similar way as for the air blast simulations. The only difference is that the relative motion of the moving rig is subtracted. Frictionless contact state is assumed. However, the influence of friction was tested with a constant friction coefficient of μ=0.1 and μ=0.2.

7 Numerical results

In this section, the numerical results representing the air blast and ground blast are presented, together with a comparison to the experiments. Primarily, frictionless contact between the target plate and the rig is assumed. The influence of a static coefficient of friction is however tested with μ=0.1 and μ=0.2. Also, a comparison between two ways of describing the blast load with considerably different complexity is included.

7.1 Air blast

This section presents the numerical results for the air blast, where the blast load has been calculated in an Eulerian domain. The simulation cases with results regarding the plate deformations for the air blast simulations are shown in Table 8. The numerical simulations show a friction dependence regarding max- and residual deformation of 1.4 % and 1.5 %, respectively, when μ=0.2 is related to frictionless state.

Table 8. Air blast simulation case descriptions with results.

Description	Max plate deformation	
	δ_{max} (mm)	δ_{res} (mm)
μ = 0	58.6	51.8
μ = 0.1	58.2	51.4
μ = 0.2	57.8	51.0

Figure 15. Numerical results for frictionless contact condition relative to the experimental results with dry surface, given with confidence bounds from the experiment.

A relative comparison between the numerical simulation with frictionless contact and the experiment with dry surface condition is shown in Figure 15. For the comparison, the average values from the experiments together with confidence bounds are used. The numerically determined quantities show a general underestimation of 10.5-11.1 % compared to the experimental averaged quantities.

Figure 16. Residual deformation along the radius measured in Test 3 with dry surface condition and the numerical simulation with frictionless contact, determined both in (a) the perpendicular and (b) diagonal direction of the plate.

In Figure 16, the profile for the residual deformation along radius for the experimental Test 3 together with numerical simulation with frictionless contact is presented, determined both to the side (a) and in the diagonal direction (b). A deviation in profile shape is shown. Figure 17

show the corresponding residual deformation modes viewed both in profile and from inside the rig.

Figure 17. The residual deformation of the target plate is viewed both in profile and from inside the rig. The plate from Test 3 is shown to the left, the simulation with frictionless contact to the right (at the simulation end time). Note that the quarter symmetry model of the plate has been reflected for better visual comparison.

7.2 Ground blast

Identical simulation cases as used for the air blast are also used for the ground blast. The results for the three simulation cases regarding the plate deformations along with the transferred impulse are shown in Table 9. The values for I_{tm} are calculated according to Eq. (1) in section 2.2, while I_{FSI} is calculated by integration of the FSI-force. The effect of the quarter symmetry in the numerical model is accounted for in the presented value for I_{FSI}.

Table 9. Ground blast simulation case descriptions with results.

Description	Max plate deformation		Test module	
	δ_{max} (mm)	δ_{res} (mm)	I_{tm} (Ns)	I_{FSI} (Ns)
$\mu = 0$	112.3	98.8	2256	2269
$\mu = 0.1$	108.8	96.9	2257	2270
$\mu = 0.2$	105.9	95.3	2258	2270

The numerical simulations show a friction dependence regarding max- and residual deformation of 5.7 % and 3.5 %, respectively, when μ=0.2 is related to the frictionless state. The corresponding relative difference regarding the test module impulse is close to zero.

Figure 18. Numerical results for frictionless contact condition relative to the experimental results, given with confidence bounds from the experiments.

The ratio between the numerical results and the experimental average results is shown in Figure 18, with confidence bounds from the experiments. All together, the numerical results underestimate the experimentally determined average values with 1.0-9.9 %. The maximum and residual deformation underestimates the experimental values with 9.4-9.9 %, respectively. The two forms of determining the transferred impulse are in close agreement with each other, and underestimate the experimental impulse only with about 1.0-1.6 %.

Figure 19. The residual deformation of the target plate viewed from inside the rig. The plate from Test 12 is shown to the left and the numerical simulation with frictionless contact to the right (at the simulation end time). Note that the quarter symmetry model of the plate has been reflected for better visual comparison.

In Figure 19, the deformation mode viewed from inside the rig is shown both for the experimental Test 12 and the simulation with frictionless contact. The deformation modes at the sides shown from the test can be recaptured in the simulation.

Figure 20. The global movement of the test module resolved in time for Test 12 and the numerical simulation with frictionless contact. Each curve maximum point is indicated with a diamond symbol.

In section 2.2 it was mentioned that the maximum vertical movement of the test module (Z_{tm}) was determined both with a linear position sensor (resolved in time) and a crush gauge, shown in Figure 3. The vertical movement of the test module for Test 12 measured with the position sensor is shown in time in Figure 20, together with the corresponding numerical simulation with frictionless contact. Time 0 s indicates the time of detonation. The measured signal of the position sensor between 3-36 ms had been corrupted by noise, hence this interval is here replaced with a dashed linear line.

7.3 Blast Model Comparison

In this section, a comparison between the two methods of describing the blast load takes place. The result from the Eulerian calculations has already been presented in section 7.1 and 7.2, while the numerical results when using the empirical blast loading function Conwep is presented here. The Conwep loading function is based on TNT charges of spherical air burst or hemi-spherical surface burst, where the explosive m/46 with mass 0.75 kg here is represented by 0.87 kg of TNT.
The air blast simulations using Conwep are simulated with spherical air burst. In Table 10, the result from the air blast simulations is given, both for the Euler- and Conwep simulations, together with the experimental results from section 2.1 with dry surface conditions. In the simulations, a frictionless contact condition was used. The maximum dynamic- and residual deformation of the plate is investigated, along with the maximum plate velocity and the total CPU-time for the numerical simulations. No maximum plate velocity was determined in the experiments, but the numerical simulations can still be compared to each other. The CPU-time for the 2D Euler simulation used to create the initial map file to fill the 3D domain is also included in Table 10.

Table 10. Blast load comparison for airblast.

Description	Max plate deformation			Plate vel.	CPU-time (s)
	δ_{max} (mm)	δ_{res} (mm)	$\delta_{max}/\delta_{res}$ (-)	v_{max} (m/s)	
Experiment	65.9	57.9	1.138	-	-
Euler 2D	-	-	-	-	15637
Euler 3D	58.6	51.8	1.131	217	14679
Conwep 0.87 kg	27.0	8.4	3.214	73	751
Conwep 3.1 kg	58.6	54.0	1.085	149	922

In Table 10, it is shown that the Conwep simulation using 0.87 kg TNT greatly under-estimates the plate deformation, compared to both the experiment and the Euler simulation. Also, the maximum plate velocity is close to 3 times lower than the corresponding Euler simulation. The Conwep TNT weight was increased to 3.1 kg in order to achieve similar maximum dynamic plate deformation as the Euler simulation. Even though the maximum deformation is equal, the residual deformation is larger for the Conwep 3.1 kg simulation compared to the Euler simulation. The ratio between the maximum dynamic- and residual plate deformation is very close to the experimental value for the Euler simulation, while the Conwep 3.1 kg simulation result in a somewhat smaller ratio. Also, the maximum plate velocity deviates about 31% for the Conwep 3.1 kg simulation compared to the Euler simulation. Regarding the CPU time, the Conwep calculations result in considerably shorter

CPU-times compared to the Euler calculations. When adding the 2D and 3D Euler CPU-times, they run 33-40 times longer than the Conwep calculations. However, the Euler 2D simulation does only have to be run once in order to create the map file, which may then be reused if more than one 3D calculation is to be performed.
Regarding the ground blast simulations, the Conwep blast loads are simulated with hemi-spherical surface burst. In addition to the quantities compared for the air blast, the transferred impulse based on the maximum test module jump is included for the ground blast comparison given in Table 11, along with the experimentally determined values from section 2.2.

Table 11. Blast load comparison for ground blast.

Description	Max plate deformation			Plate vel.	Test Module	CPU-time (s)
	δ_{max} (mm)	δ_{res} (mm)	$\delta_{max}/\delta_{res}$ (-)	v_{max} (m/s)	I_{tm} (Ns)	
Experiment	124.0	109.7	1.130	-	2293	-
Euler 2D	-	-	-	-	-	10915
Euler 3D	112.3	98.8	1.134	277	2256	69387
Conwep 0.87 kg	37.0	22.6	1.637	95	1306	1652
Conwep 3.9 kg	112.4	94.9	1.184	221	4087	1842

Similar to the air blast comparison, the Conwep simulation using 0.87 kg TNT greatly underestimates the plate deformation, compared to both the experiment and the Euler simulation. In general, similar deviation between the results is experienced for the ground blast comparison as for the air blast comparison. The hemi-spherical charge when using Conwep was increased to 3.9 kg TNT in order to correlate the maximum dynamic plate deformation to the Euler calculation. The residual deformation then resulted in a smaller value compared to the Euler calculation, in contrast to the increased Conwep charge for the air blast comparison. The maximum plate velocity is smaller for the Conwep 3.9 kg simulation than the Euler simulation, but the deviation is not as large as the corresponding air blast comparison. The ratio between the maximum dynamic- and residual plate deformation is very close to the experimental value for the Euler simulation, while the Conwep 3.9 kg simulation results in a slightly larger ratio. The transferred impulse deviates between 42-81 % for the two Conwep simulations compared to the Euler simulation. The Euler simulation for the transferred impulse is however in very good agreement with the experiment. When adding the 2D and 3D Euler CPU-times, they run 44-49 times longer than the Conwep calculations.

8. Discussion and conclusion

Numerical simulations with comparison to two types of blast experiments have been carried out; air blast with explosive placed in free air and ground blast with explosive placed in a steel pot. Structural deformation of steel plates were measured, both the maximum dynamic- and residual deformation. For the ground blast, also the transferred impulse was determined. The primary aim with this work has been to investigate the sensitivity and accuracy of simulating the blast load using an Eulerian domain. Further, a comparison between using an empirical blast loading function and the more complex Eulerian calculations to describe the blast load has also been made, both regarding structural deformation as well as CPU time.

The numerical results regarding the plate deformations underestimated the experimental values with a bound of 9.4-11.1 %, for the two presented blast setups. Regarding the impulse transfer for the ground blast, the numerical underestimation compared to the test results is only between 1.0-1.6 %. The underestimation is most likely a result of many combining

factors. Although a convergence study is carried out within this work, the largest error contributor is probably the numerical simulations regarding the gas dynamics. Experimental uncertainties are also present. For example, while ideal symmetry is assumed in the numerical models, some deviation in the field tests regarding the vertical alignment between plate and charge centre along with the charge initiation point exist. Also, the friction for the steel/steel contact in the experiments is unknown, and is most likely not constant nor zero. An influence of friction is observed regarding the plate deformation in the air blast experiments. The numerical simulations show that the influence of friction is small regarding the impulse transfer, but has a larger influence on the plate deformation. Considering the influence of friction, the reported underestimation of the plate deformation is likely to be a few percent higher if an accurate friction model is included. The material parameters regarding Weldox 700E for the modified JC model is based on material testing by Børvik et al. [16]. A modification of the strain rate parameters to better match the strain rate testing from the reference has been done to this work. The initial yield limit of Weldox 700E differs between 785 MPa, 819 MPa and 859 MPa between three references where the material has been characterised [32,16,33]. Since there appears to be quite a difference in initial yield strength between different batches of the same material quality, the material parameters of the target plate could still be a minor contribution to the numerical underestimation. The parameters for the explosive m/46 has not been widely validated, but the parameters are an empirical fit to cylinder tests that covers the relative volumes of gas expansion experienced in this work. However, no material parameter validation to explosions of m/46 in air has been performed in this study, and may thus also be a small contributor to the error.

The two methods of describing the blast load resulted in completely different results. In general, equal explosive weight result in much smaller deformation for the Conwep calculations than the corresponding Euler calculations. The most obvious reason for the deviation is the difference in explosive shape, since the actual cylindrical shape used in the experiments is simulated in the Euler calculations, while Conwep is based on spherical – or hemispherical explosive shapes. Further, the explosive confinement is tremendously different between the two models regarding the ground blast. In the Euler calculations, the explosive was positioned in a steel pot, while the blast load in the Conwep model was based on a hemispherical explosive shape placed on the ground. If the explosive size in the Conwep models is increased to reach the same maximum dynamic plate deformations as in the Euler calculations, the residual plate deformation, maximum plate velocity and transferred impulse still deviate from the corresponding Euler simulation. The largest deviation (between 40-80 %) is seen regarding the impulse transfer. Also, the ratio between the maximum dynamic- and residual plate deformation is close to identical for the Euler simulations and the experiments, while the Conwep models show a larger deviation. This may indicate that the actual shape of the gas dynamics in the Euler calculations is rather well represented, assuming that the material data for the target plate is accurate. The CPU time for the Euler calculations exceeds the Conwep calculations by a factor of 40-50 times. If one can accept the limitations of the Conwep model, it may thus be a time effective approach to use in a concept study. However, for more accurate description of the blast load, the Euler model would be the obvious choice.

All together, with use of initial fine grid model in 2D and mapping to a coarse 3D model with biased element distribution, reasonable numerical results and model sizes can be achieved from near-field explosions in air.

9. Acknowledgements

The authors are truly grateful to the Swedish Defence Research Agency, FOI, for the cooperation with BAE Systems Hägglunds AB which resulted in the development of the air- and ground blast rig, along with the following experimental work.

References

[1] AEP-55 Procedures for evaluating the protection level of logistic and light armored vehicles., Vol. 2, 1st ed., NATO, 2006.
[2] B. Gel'fand, I. Voskoboinikov, S. Khomik, Recording the position of a blast-wave front in air, Combustion, Explosion, and Shock Waves. 40 (2004) 734-736.
[3] E.D. Esparza, Blast measurements and equivalency for spherical charges at small scaled distances, International Journal of Impact Engineering. 4 (1986) 23-40.
[4] C.N. Kingery, G. Bulmash, Airblast parameters from TNT spherical air burst and hemispherical surface burst, ARBRL-TR-02555, U.S. Army Ballistic Research Laboratory, Aberdeen Proving Ground, MD, 1984.
[5] G. Randers-Pehrson, K. Bannister, Airblast loading model for DYNA2D and DYNA3D, ARL-TR-1310, Army Research Laboratory, 1997.
[6] J.O. Hallquist, LS-DYNA Keyword user's manual, Version 971 / Rev 5 (Beta), Livermore Software Technology Corporation, 2010.
[7] A. Neuberger, S. Peles, D. Rittel, Springback of circular clamped armor steel plates subjected to spherical air-blast loading, International Journal of Impact Engineering. 36 (2009) 53-60.
[8] A. Wenzel, E.D. Esparza, Pressure and impulse measurements close to explosions in air and in earth, ISA Transactions. (1974) 212-225.
[9] S.C.K. Yuen, G.N. Nurick, Experimental and numerical studies on the response of quadrangular stiffened plates. Part I: Subjected to uniform blast load, International Journal of Impact Engineering. 31 (2005) 55-83.
[10] G.S. Langdon, S.C.K. Yuen, G.N. Nurick, Experimental and numerical studies on the response of quadrangular stiffened plates. Part II: Localised blast loading, International Journal of Impact Engineering. 31 (2005) 85-111.
[11] M.S. Chafi, G. Karami, M. Ziejewski, Numerical analysis of blast-induced wave propagation using FSI and ALE multi-material formulations, International Journal of Impact Engineering. 36 (2009) 1269-1275.
[12] A. Neuberger, S. Peles, D. Rittel, Scaling the response of circular plates subjected to large and close-range spherical explosions. Part I: Air-blast loading, International Journal of Impact Engineering. 34 (2007) 859-873.
[13] D. Karagiozova, G. Langdon, G. Nurick, S. Chung Kim Yuen, Simulation of the response of fibre-metal laminates to localised blast loading, International Journal of Impact Engineering. 37 (2010) 766-782.
[14] J.A. Zukas, D.R. Scheffler, Practical aspects of numerical simulations of dynamic events: effects of meshing, International Journal of Impact Engineering. 24 (2000) 925-945.
[15] B. Zakrisson, B. Wikman, B. Johansson, Half scale experiments with rig for measuring structural deformation and impulse transfer from land mines, in: 24th International Symposium on Ballistics, DEStech Publications, Inc, 2008: pp. 497-504.
[16] T. Børvik, S. Dey, A. Clausen, Perforation resistance of five different high-strength steel plates subjected to small-arms projectiles, International Journal of Impact Engineering.

36 (2009) 948-964.
[17] D.J. Benson, Computational methods in Lagrangian and Eulerian hydrocodes, Computer Methods in Applied Mechanics and Engineering. 99 (1992) 235-394.
[18] T. Børvik, A. Hanssen, M. Langseth, L. Olovsson, Response of structures to planar blast loads - A finite element engineering approach, Computers & Structures. 87 (2009) 507-520.
[19] J.A. Zukas, Introduction to hydrocodes, 1st ed., Elsevier Science, 2004.
[20] J.O. Hallquist, LS-DYNA Theory manual, Livermore Software Technology Corporation, 2006.
[21] T.C. Chapman, T.A. Rose, P.D. Smith, Blast wave simulation using AUTODYN2D: A parametric study, International Journal of Impact Engineering. 16 (1995) 777-787.
[22] C. Tham, Numerical simulation on the interaction of blast waves with a series of aluminum cylinders at near-field, International Journal of Impact Engineering. 36 (2009) 122-131.
[23] N. Aquelet, M. Souli, 2D to 3D ALE Mappping, in: 10th International LS-DYNA Users Conference, Detroit, 2008.
[24] V. Lapoujade, N. Van Dorsselaer, S. Kevorkian, K. Cheval, A study of mapping technique for air blast modeling, in: 11th International LS-DYNA Users Conference, Detroit, 2010.
[25] A. Helte, J. Lundgren, H. Örnhed, M. Norrefeldt, Evaluation of performance of m/46 (in Swedish), FOI-R--2051--SE, Swedish Defence Research Agency, 2006.
[26] W.E. Baker, J.J. Kulesz, P.S. Westine, P.A. Cox, J.S. Wilbeck, A manual for the prediction of blast and fragment loading on structures, Southwest Research Inst. San Antonio TX USA, 1981.
[27] R.E. Sonntag, C. Borgnakke, G.J. Van Wylen, Fundamentals of thermodynamics, 6th ed., New York, Wiley, cop., 2003.
[28] T. Børvik, O. Hopperstad, T. Berstad, M. Langseth, A computational model of viscoplasticity and ductile damage for impact and penetration, European Journal of Mechanics. A, Solids. 20 (2001) 685-712.
[29] I.B. Celik, U. Ghia, P.J. Roache, C.J. Freitas, Procedure for estimation and reporting of uncertainty due to discretization in CFD applications, Trans. ASME J. Fluids Eng. 130 (2008) 0708001.
[30] L.E. Schwer, Is your mesh refined enough? Estimating discretization error using GCI, in: LS-DYNA Forum, Bamberg, Germany, 2008.
[31] C. Elfving, The effect of ground reflection (in Swedish), FOA-R-95-00135-6(2.6)--SE, National Defence Research Establishment, 1995.
[32] M. Clarin, High strength steel - Local buckling and residual stresses, Licentiate Thesis, Luleå University of Technology, 2004.
[33] S. Dey, T. Børvik, O. Hopperstad, M. Langseth, On the influence of fracture criterion in projectile impact of steel plates, Computational Materials Science. 38 (2006) 176-191.

Figure 1

Click here to download high resolution image

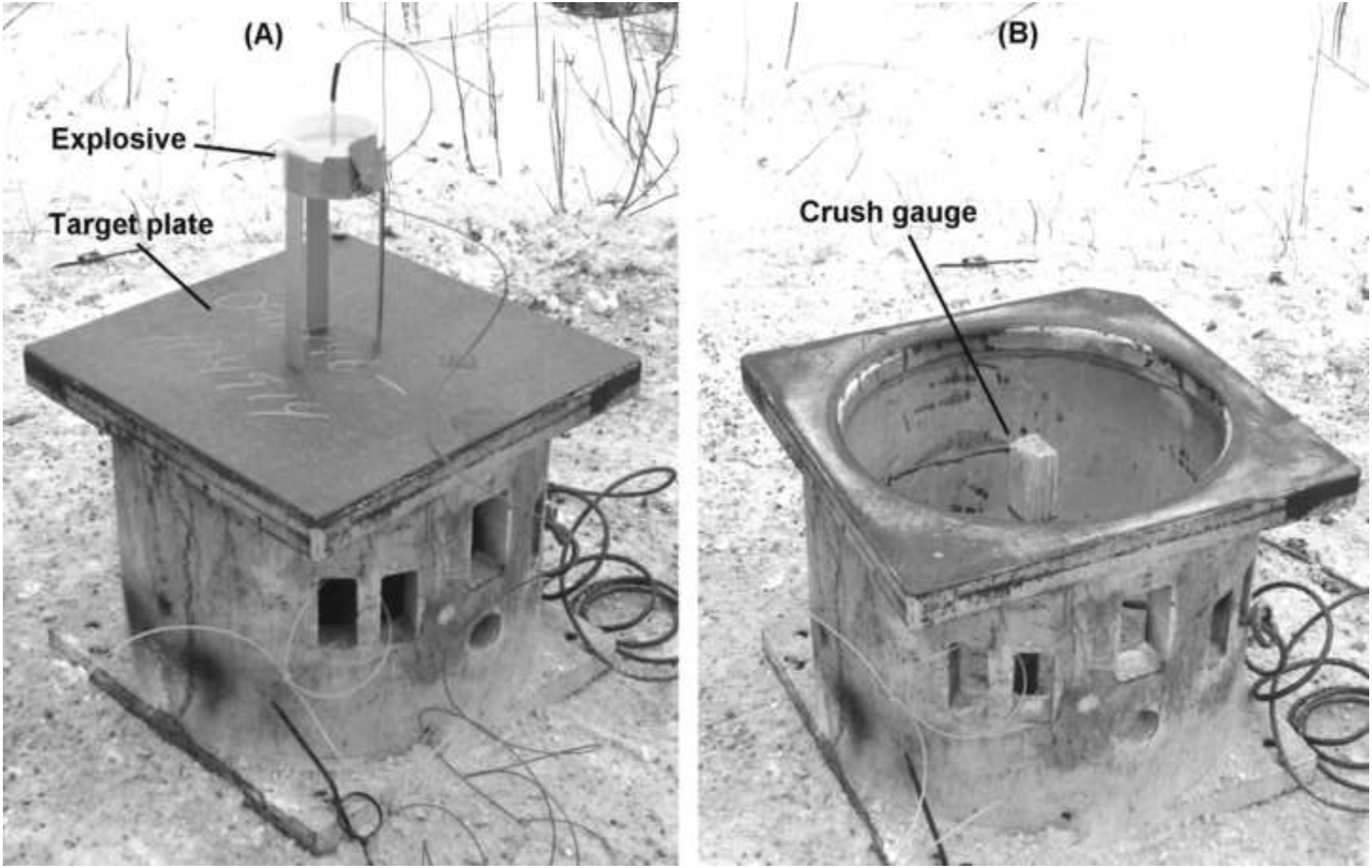

Figure 2

Click here to download high resolution image

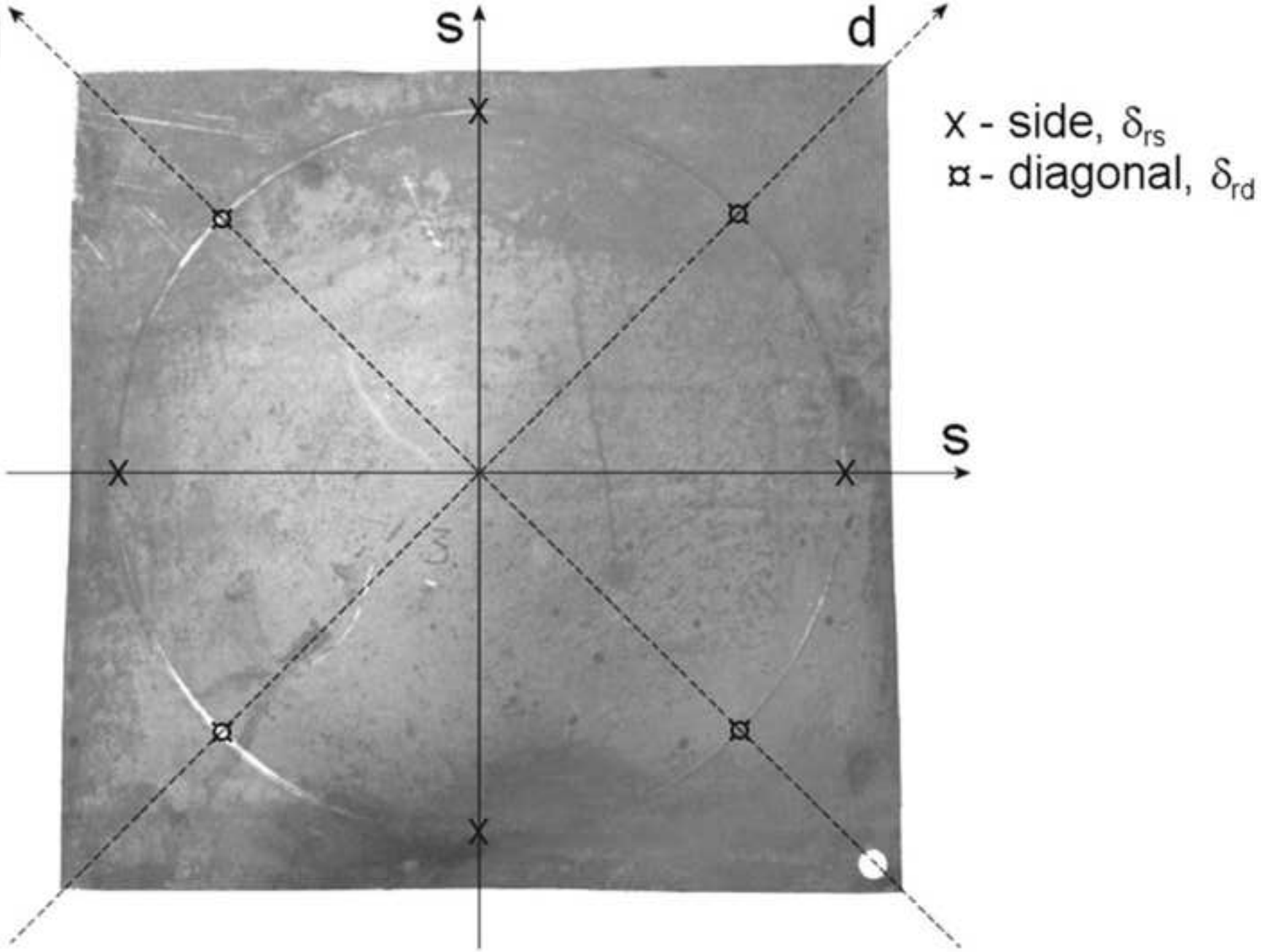

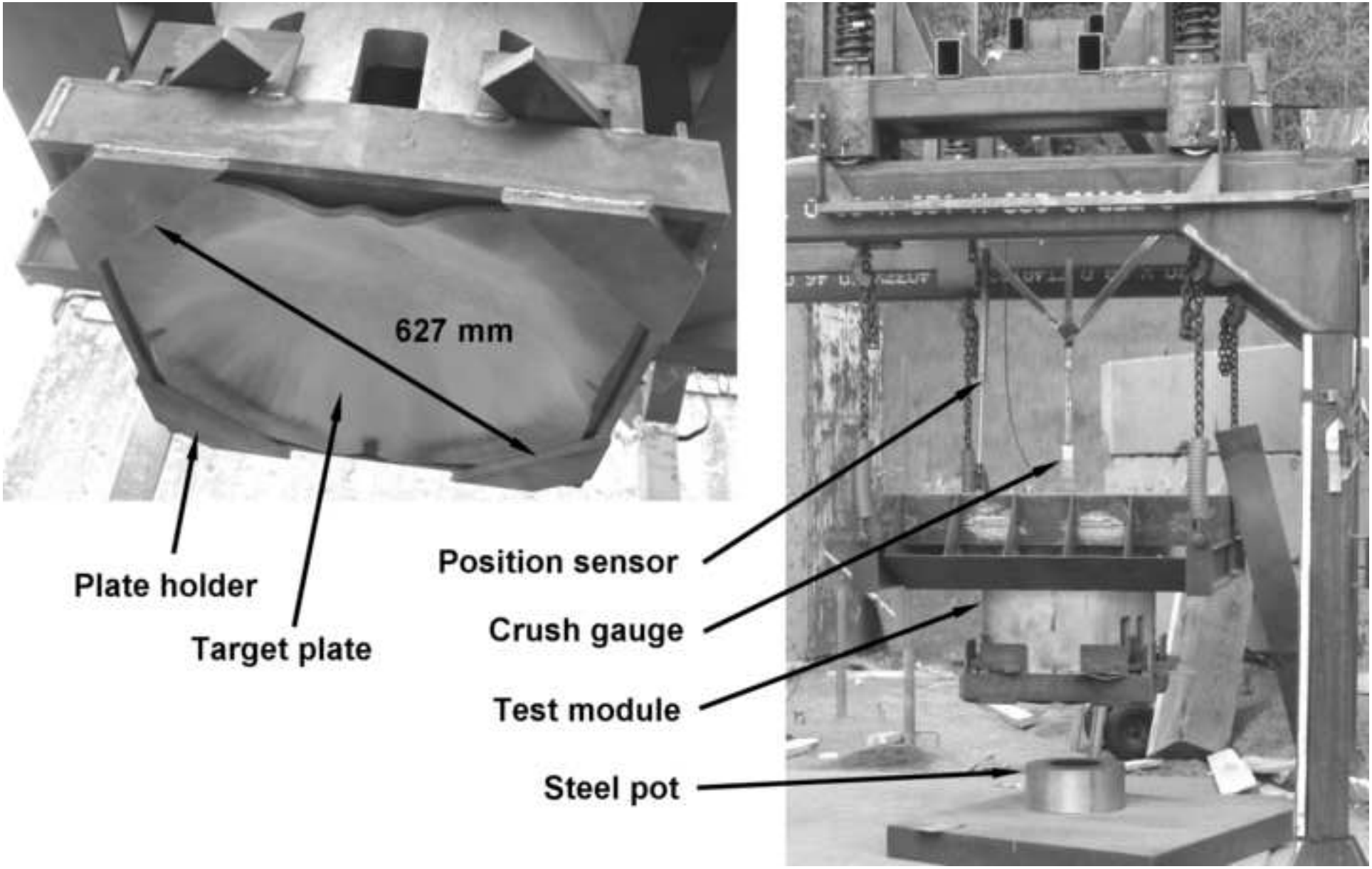

Figure 4

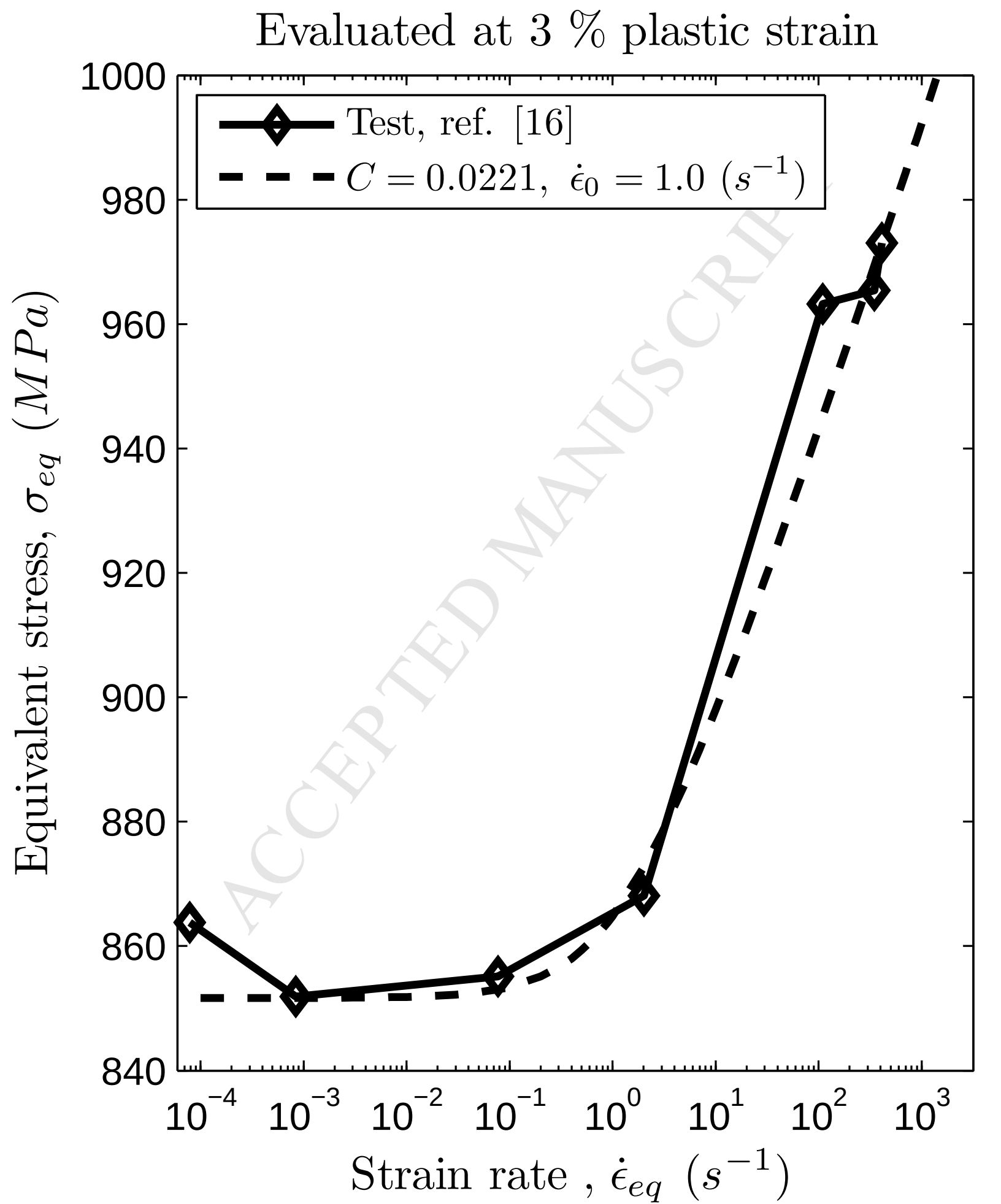

Figure 5

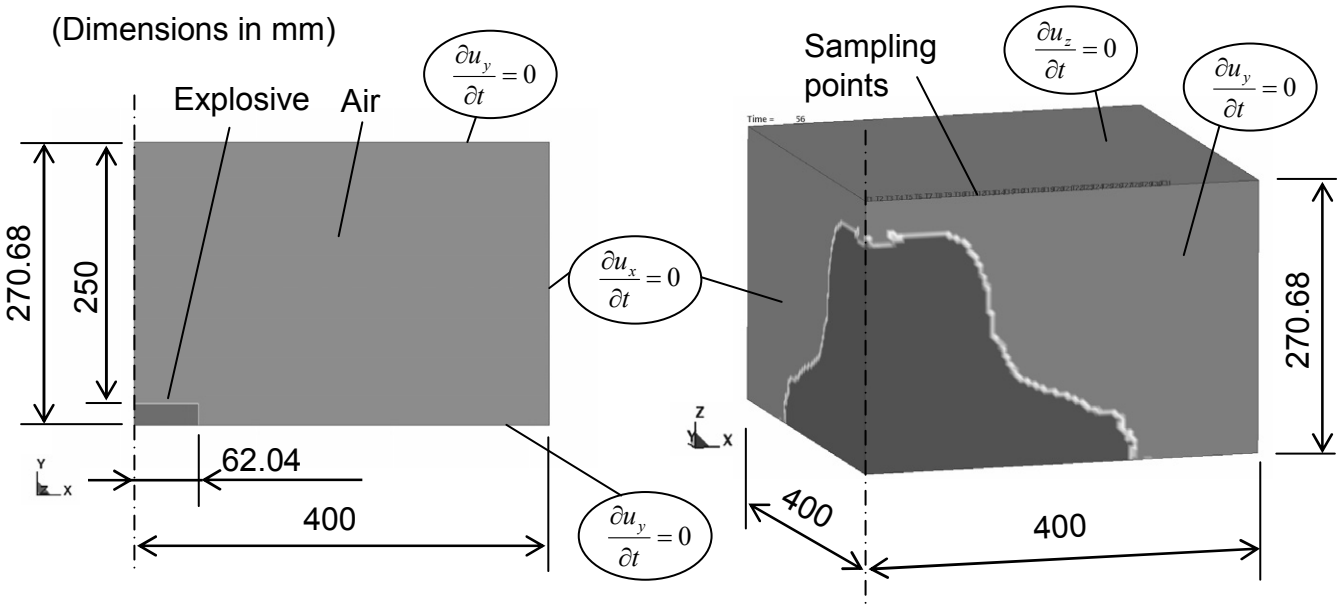

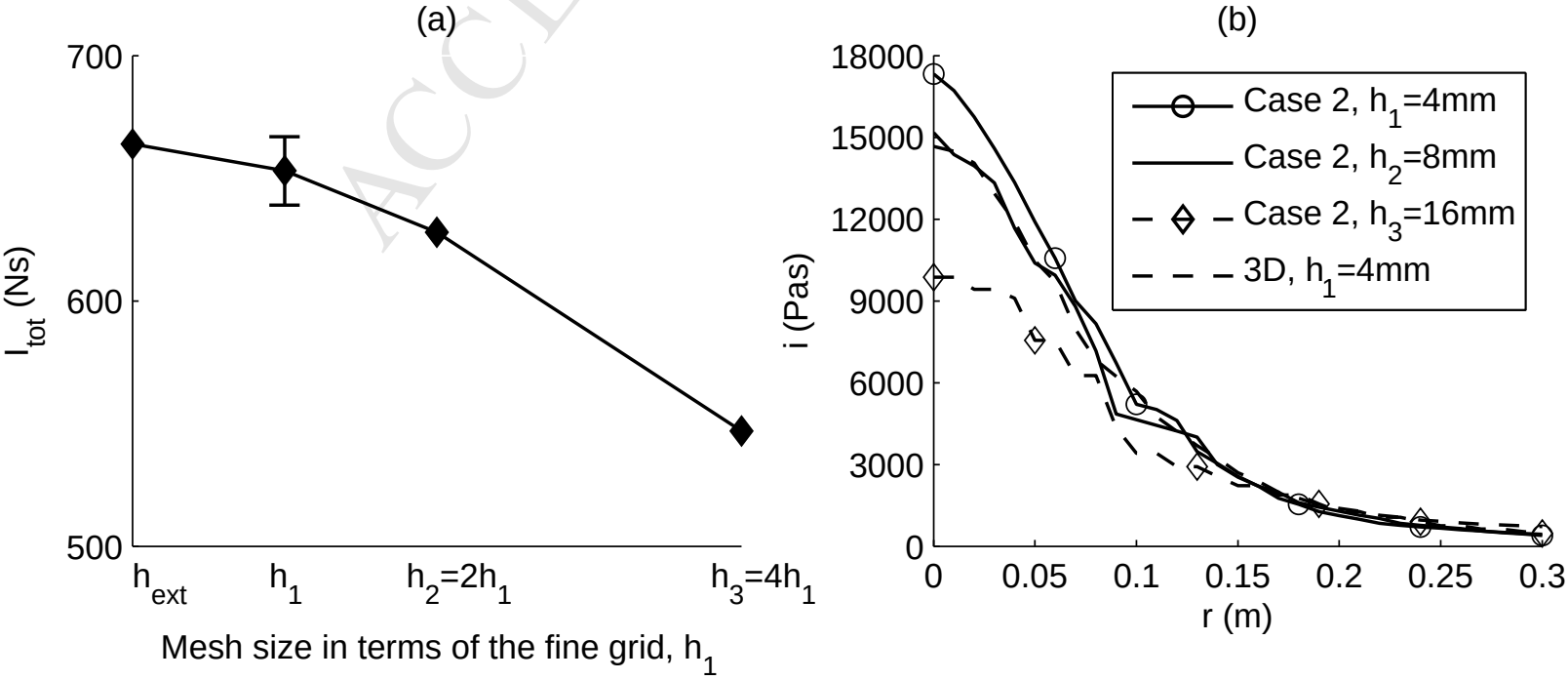

Figure 7

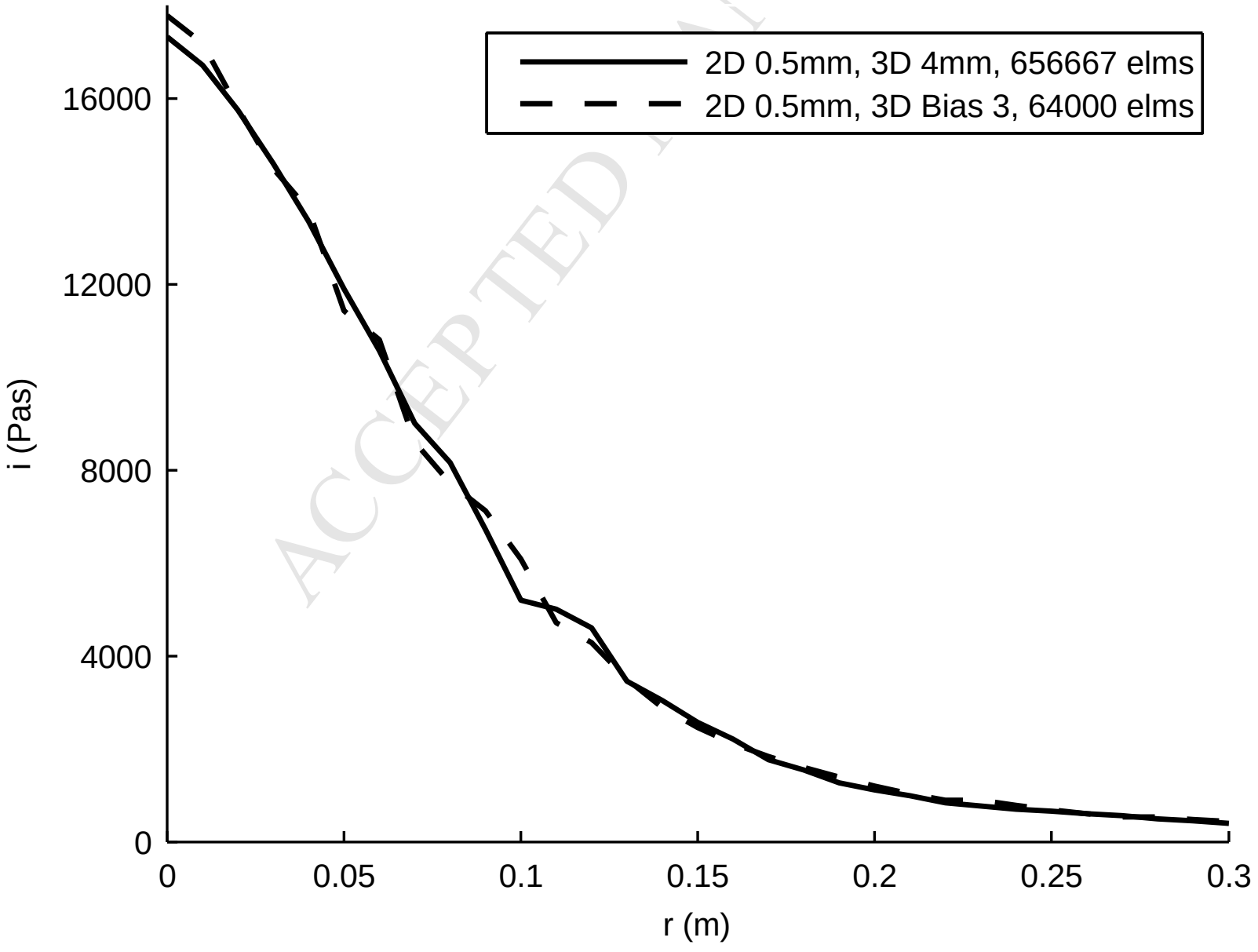

Figure 8

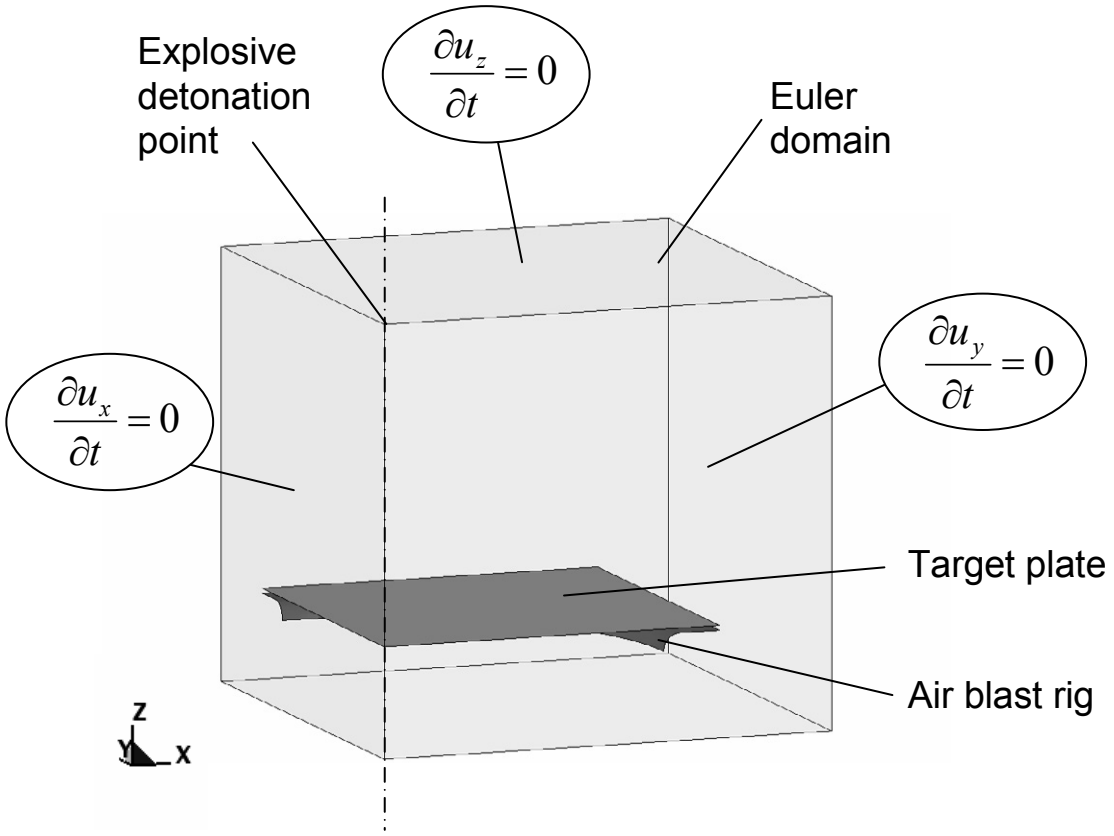

Figure 9

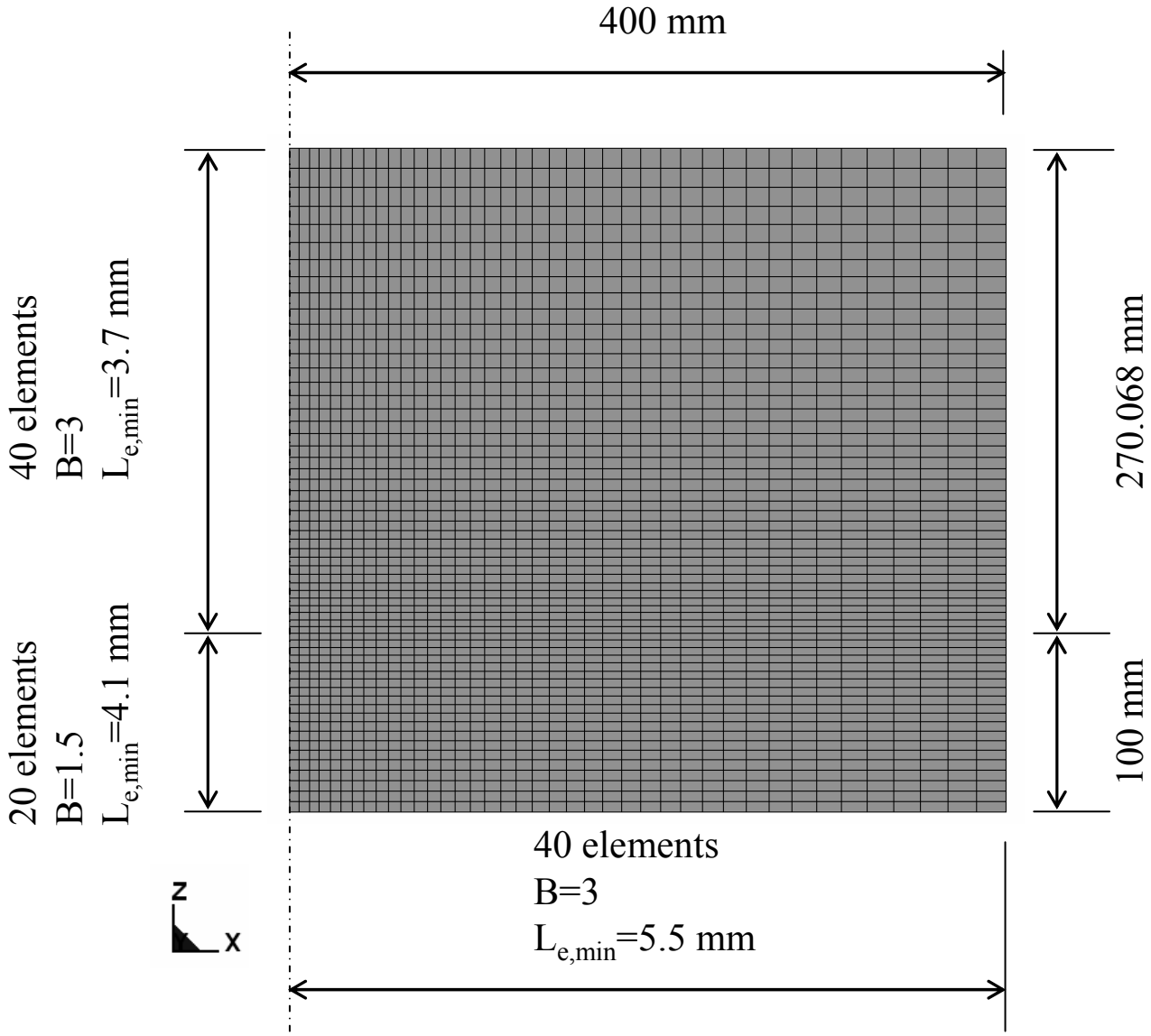

Figure 10

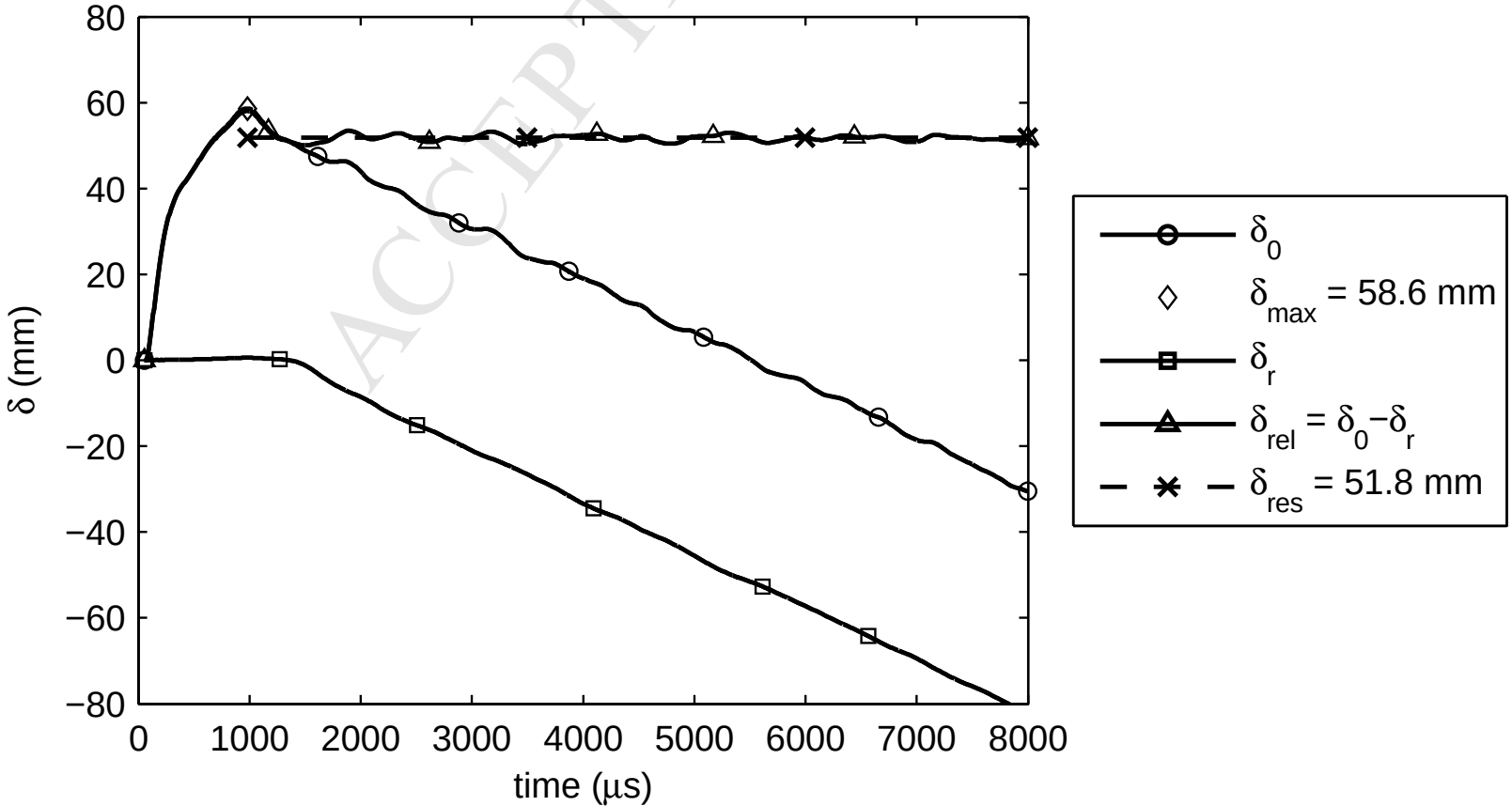

Figure 11

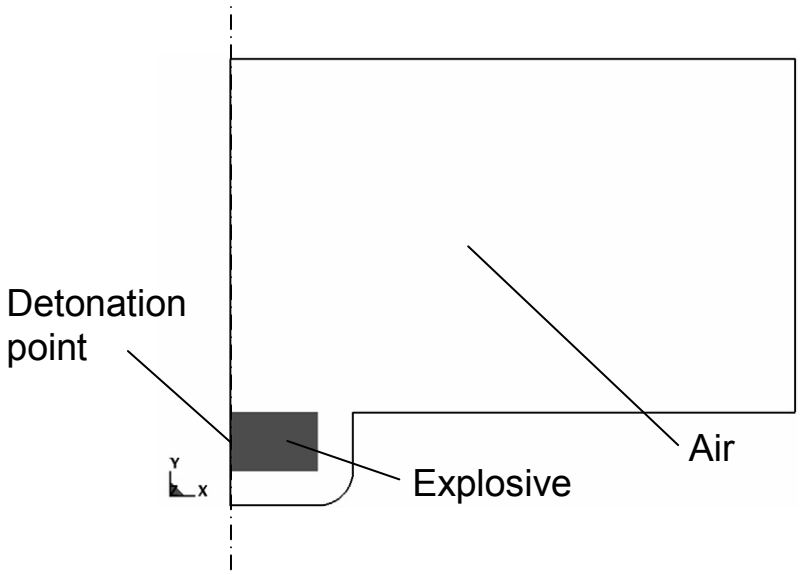

Figure 12

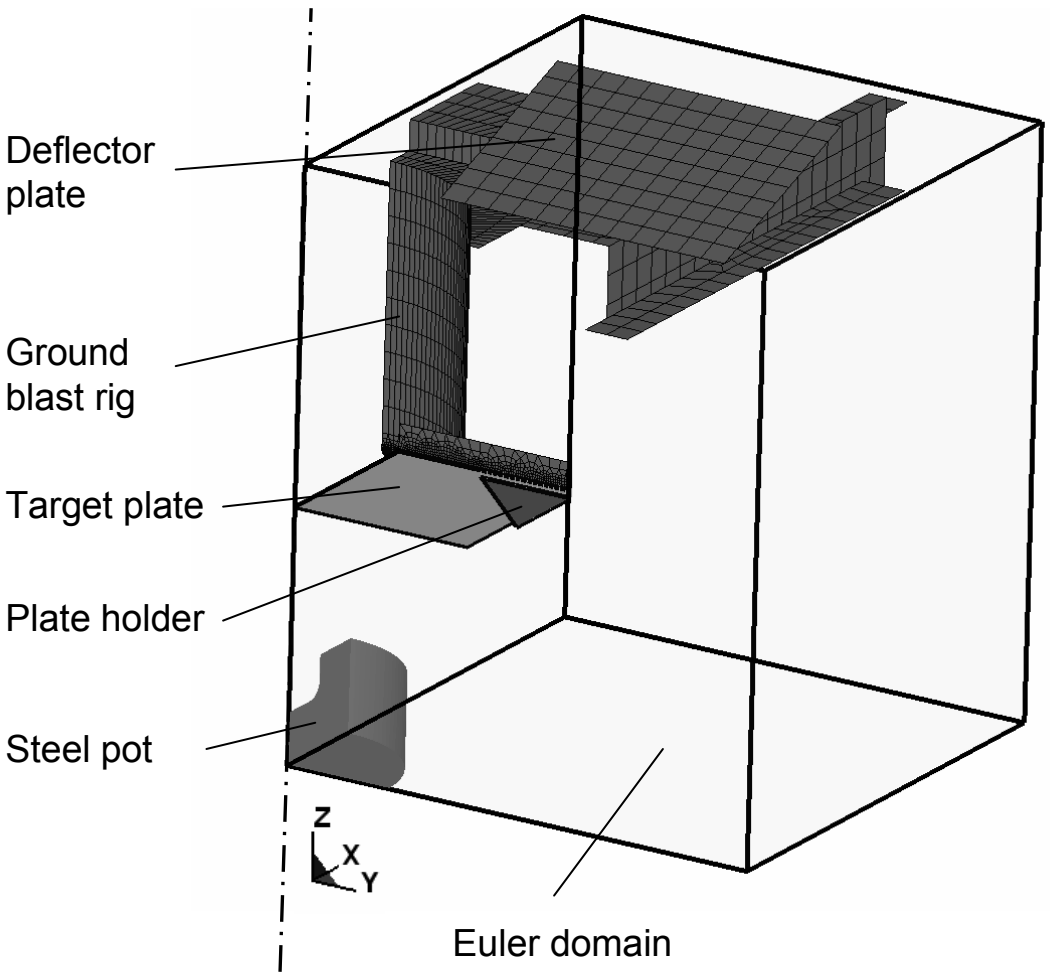

Figure 13

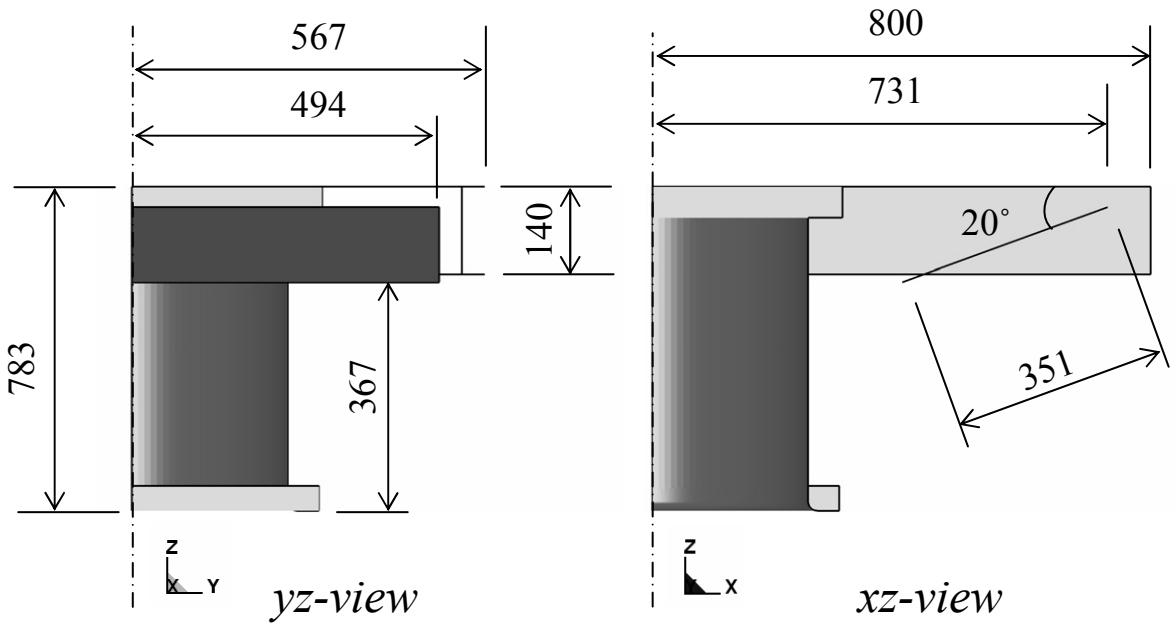

Figure 14

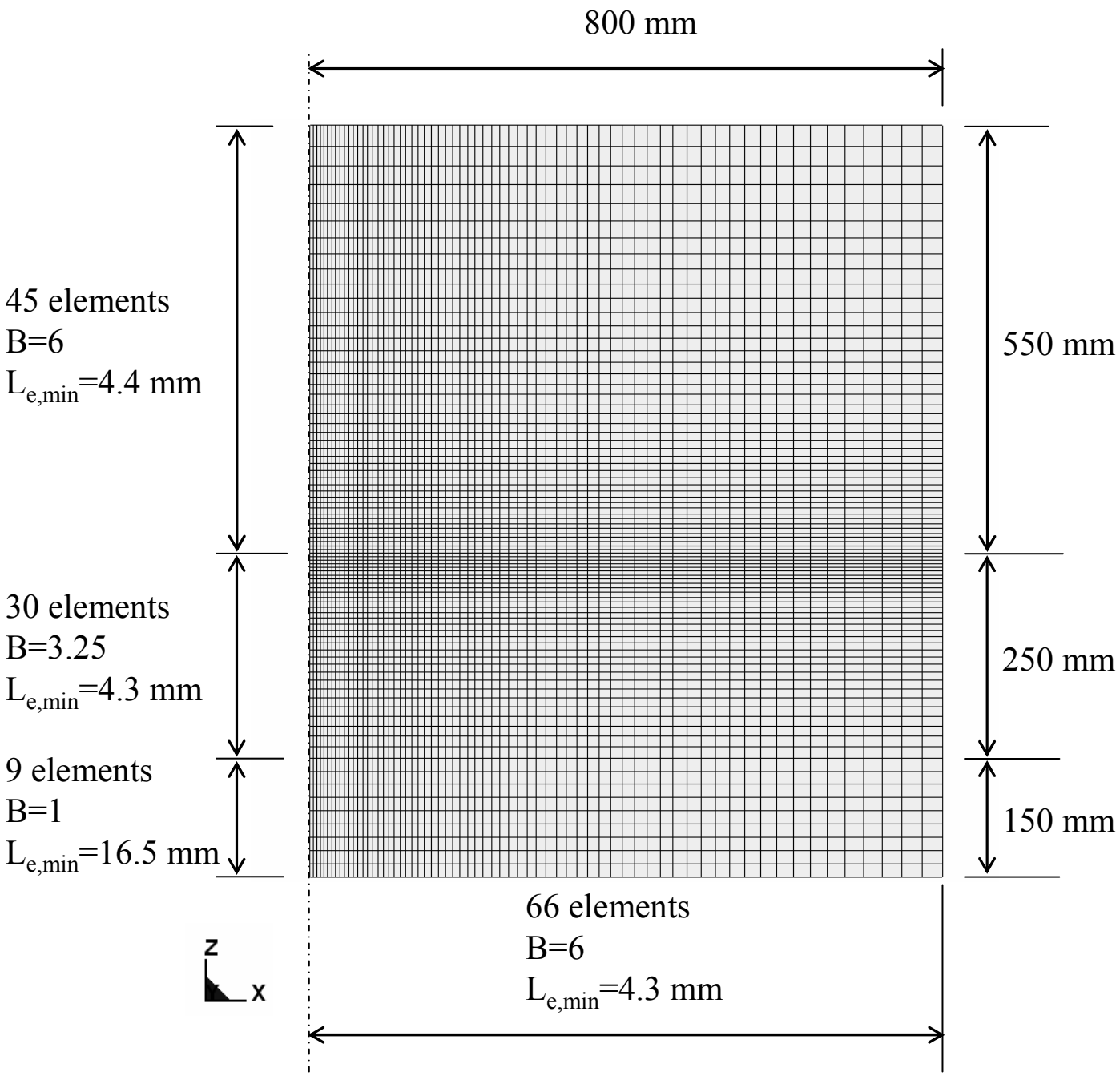

Figure 15

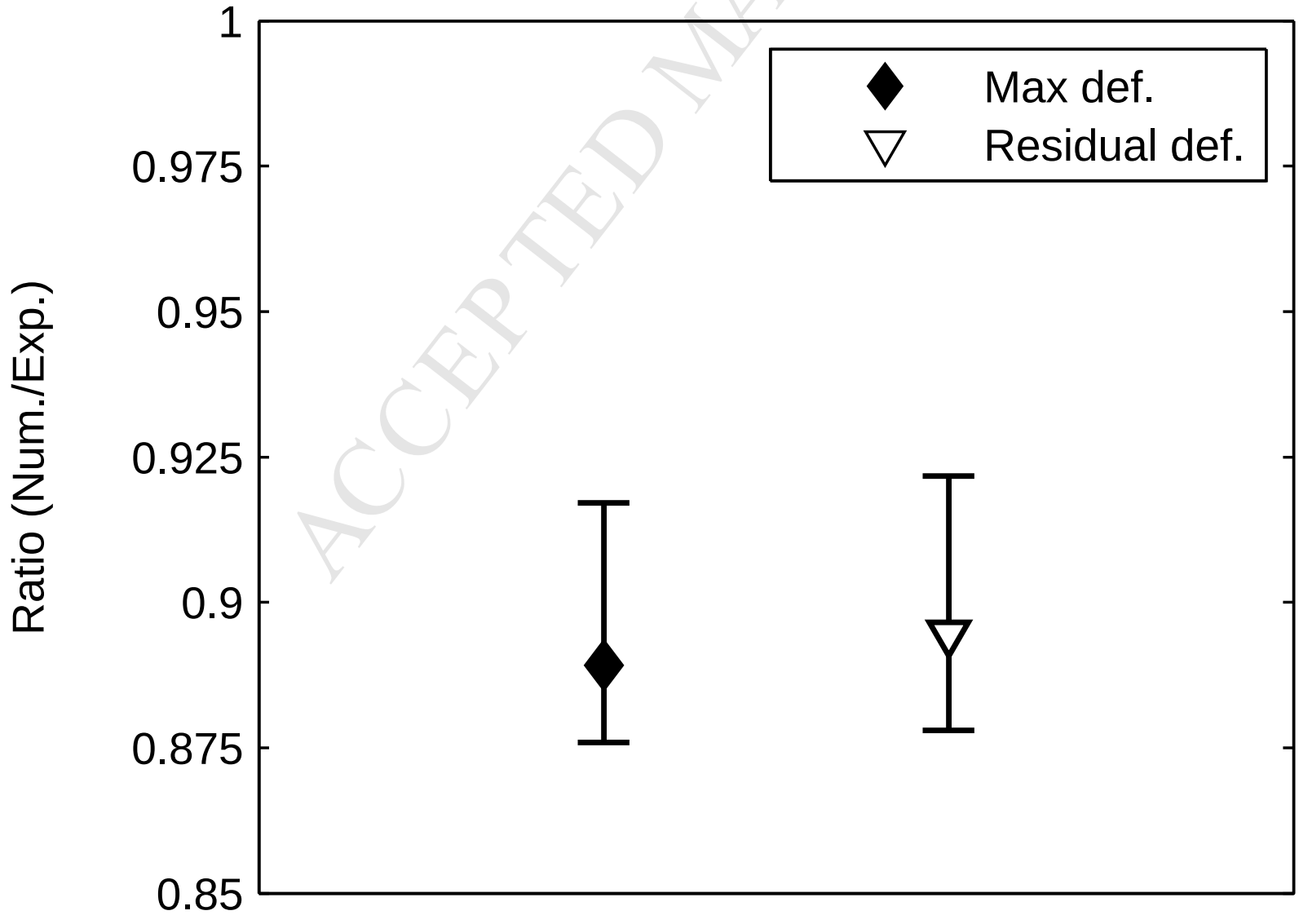

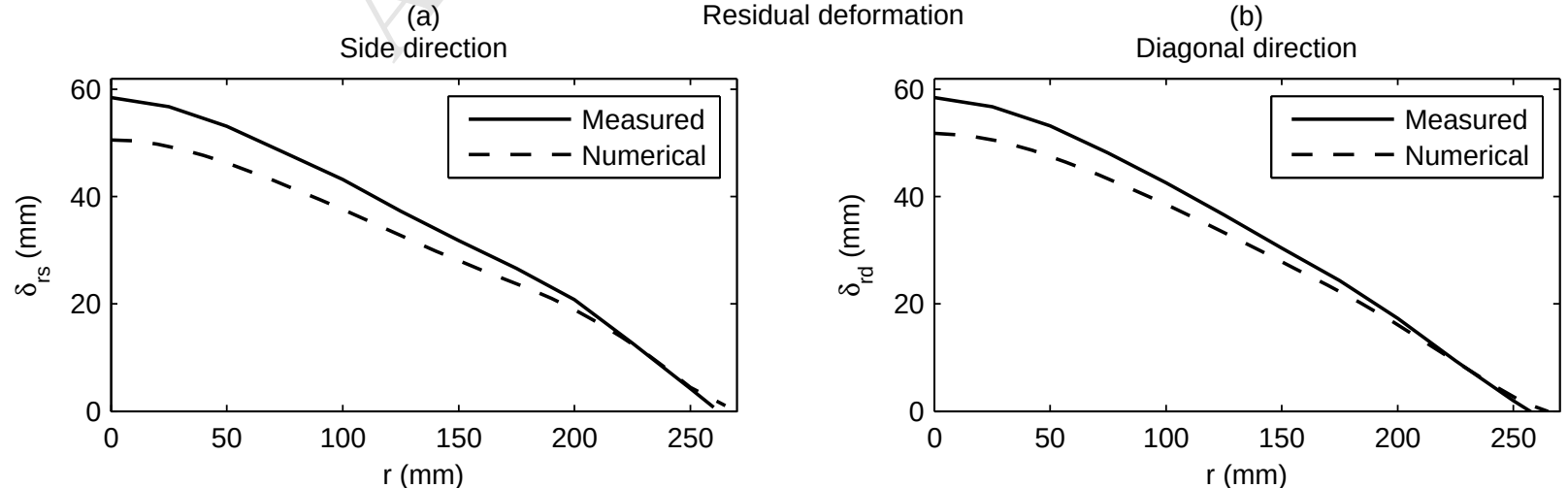

Figure 17

Click here to download high resolution image

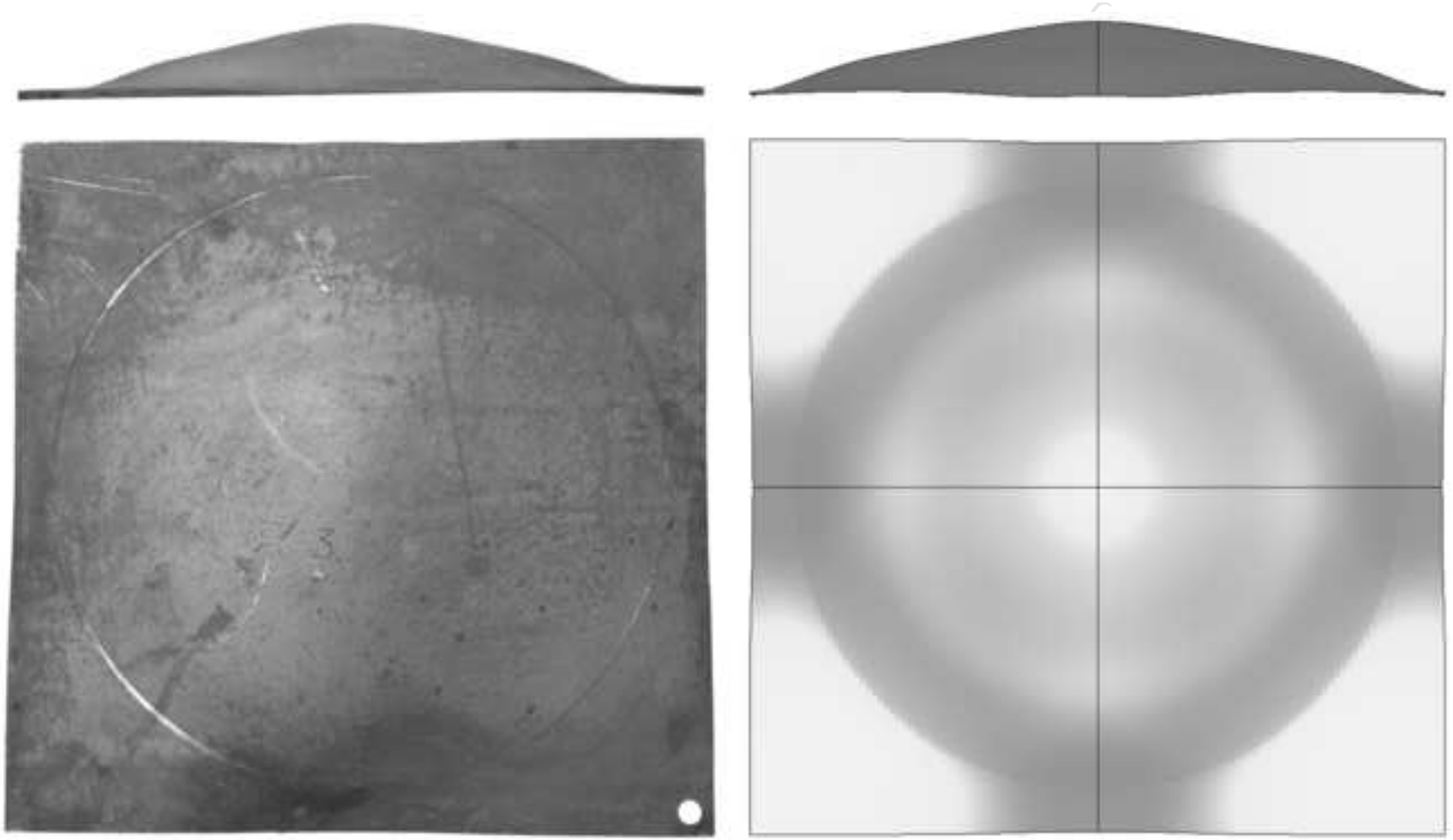

Figure 18

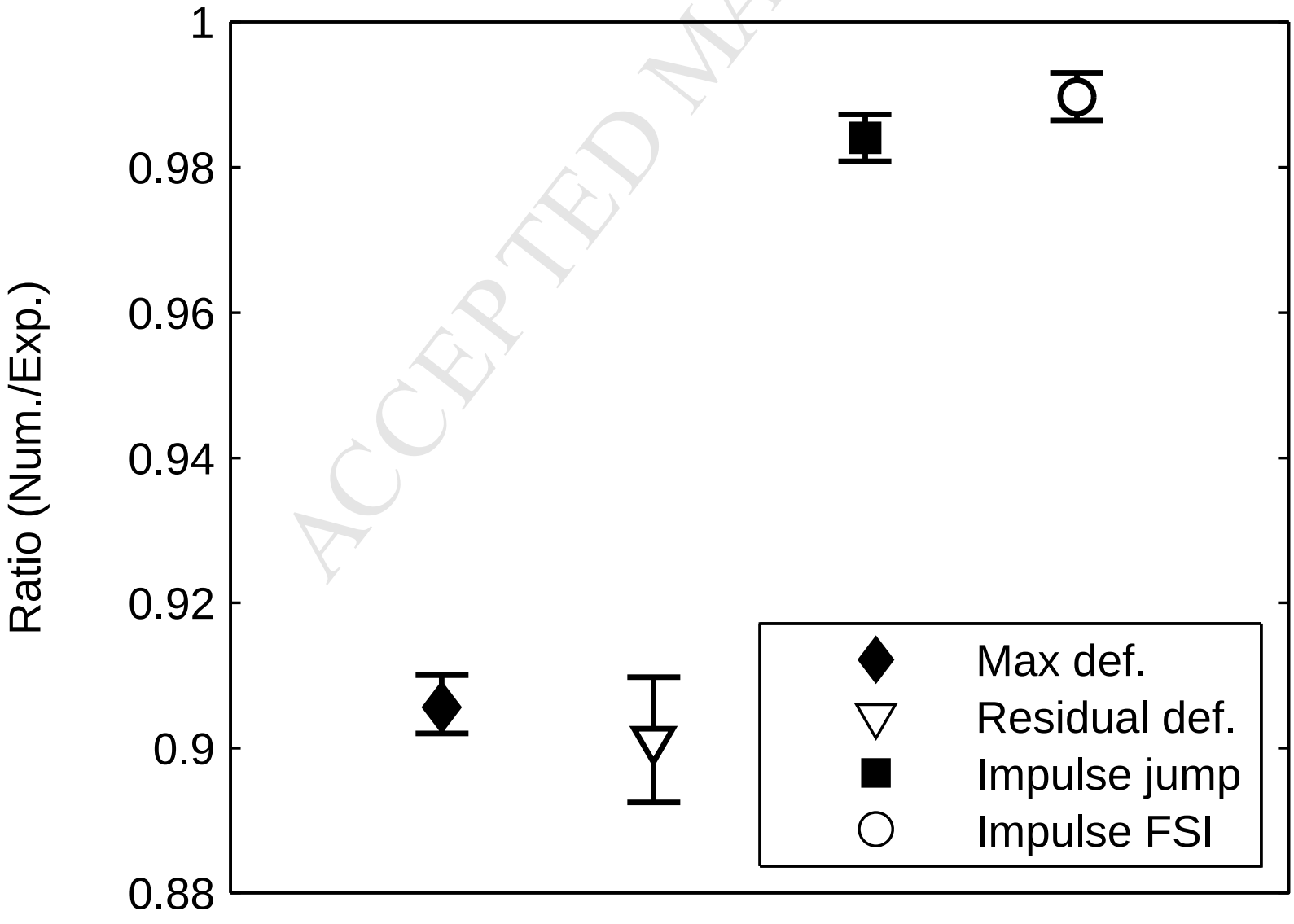

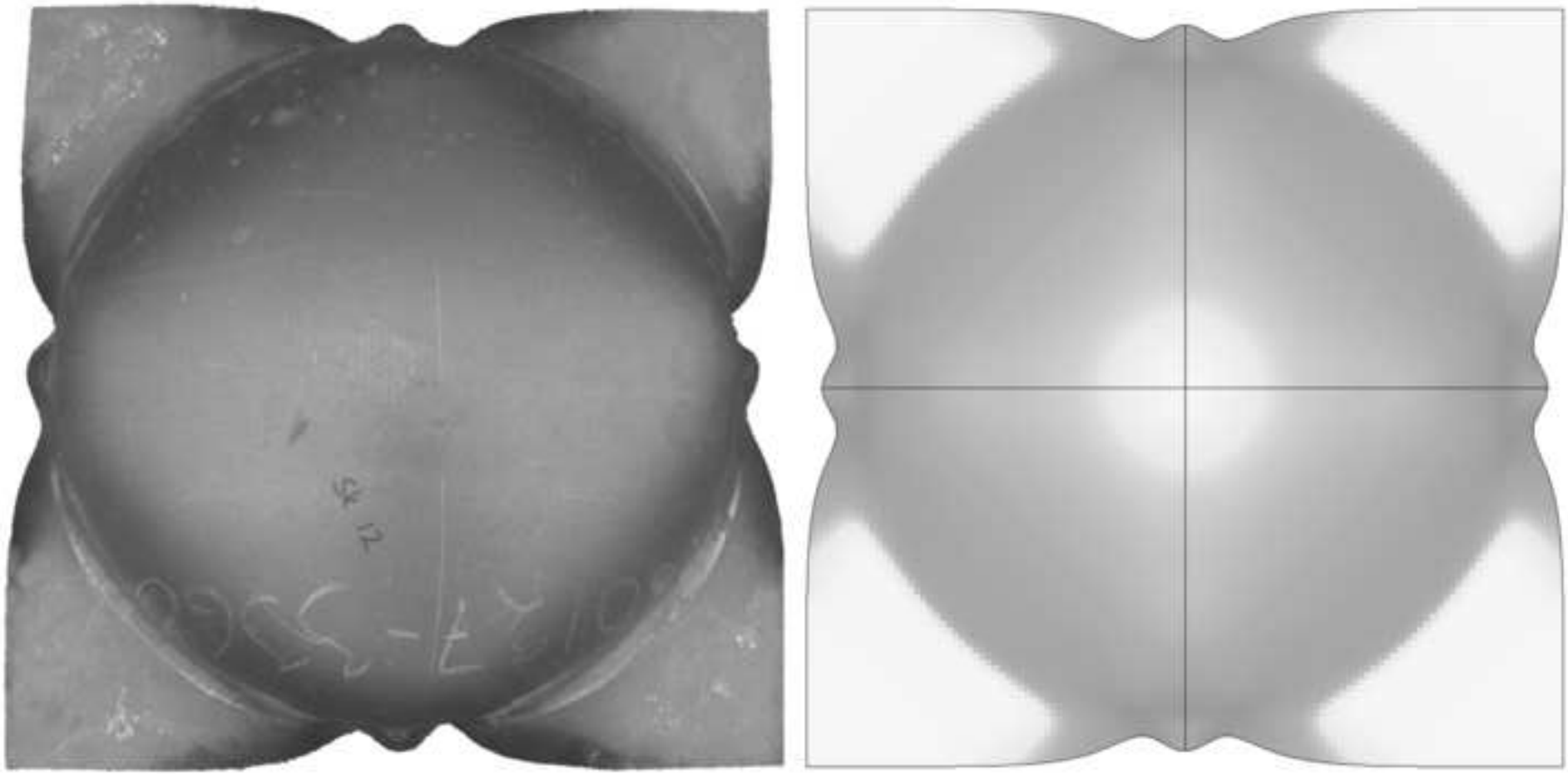

Figure 20